POLITECNICO DI TORINO

Corso di Laurea Magistrale in

INGEGNERIA ENERGETICA E NUCLEARE

Master Thesis

Qualification of Tritium Extraction System from Pb-15.7Li in TRIEX-II Facility

Advisor
Prof. M. Zucchetti

Candidate
Mattia Cantore

Co-advisors
Eng. R. Testoni
Eng. L. Candido
Eng. M. Utili

Academic Year 2018/2019

Abstract

The purpose of this work is to characterise the tritium extraction from lithium-lead with GLC. In particular, the packed column technology installed on TRIEX-II facility, built in C. R. ENEA Brasimone, has been analysed. The construction phase and the experimental campaign of the facility have been followed during the past months. A 0D model was developed for the PbLi loop of the facility, analysing the mass balance of the system and the permeation fluxes through the piping involved in the tests. Moreover, the performances of the permeation sensors installed for the hydrogen concentration measurements, developed at C. R. ENEA Brasimone, has been tested. A 2D model for their characterisation in gas phase has been built and compared with the results, keeping into account the previous experimental campaign aimed for their qualification on Hyper-Quarch device.

Sommario

Lo scopo di questo lavoro è di caratterizzare l'estrazione del trizio dal PbLi con GLC. In particolare, è stata analizzata la tecnologia della colonna a riempimento installata sull' impianto TRIEX-II, costruito al C. R. ENEA Brasimone. La fase di costruzione e la campagna sperimentale sono state seguite di persona durante gli scorsi mesi. Un modello 0D è stato sviluppato per il circuito PbLi della struttura, analizzando il bilancio di massa del sistema e i flussi di permeazione attraverso le tubazioni. Inoltre, sono state testate le prestazioni dei sensori a permeazione installati per misurare la concentrazione di idrogeno nel PbLi, sviluppati presso C.R. ENEA Brasimone. Un modello 2D per la loro caratterizzazione in fase gas è stato costruito e confrontato con i risultati, tenendo conto della precedente campagna sperimentale finalizzata alla loro qualificazione con il dispositivo Hyper-Quarch.

Acknowledgements

I want to thank my research supervisor, Eng. Marco Utili, for his guidance during these months of work and the help in the most difficult parts of the job. I would like to thank my thesis advisor, Prof. Massimo Zucchetti, for the opportunity he gave me and my co-advisors, Eng. Luigi Candido and Eng. Raffaella Testoni, for their continuous support during these months and during the writing of the thesis. Regarding the work period carried out in ENEA, I would like to thank all the colleagues that I knew, for their help and for the very good time that I spent with them. Thanks also to my colleague Edoardo Galli, who endured me during these months of living together and with whom I spent many beautiful funny moments.

I want to thank also my mother, for her support in these difficult years and for the trust she had in me in this study period.

Last but not least, a special thanks to Alessia, my love and my life partner, who supported me in the darkest moments and always believed in me giving me the strength to continue. Everything is less hard when we are together.

Contents

1 Introduction 10

2 Fusion basics and engineering 12

2.1 Physical process 12

2.2 ITER and DEMO projects 15

2.2.1 Tokamak device 16

2.2.2 ITER 17

2.2.3 DEMO 26

2.3 Tritium technologies: extraction from breeding blanket and permeation phenomena 30

3 Hyper-Quarch 36

3.1 Hyper-Quarch: layout and results 36

3.2 Permeation sensors 38

3.3 Mathematical description of gas phase model 42

3.4 Results and discussion 45

3.5 Solubility measurement: Hyper-Quarch-II 48

4 Characterisation of Tritium Extraction System 51

4.1 Gas Liquid Contactor 51

4.1.1 Packed column design 54

4.2 TRIEX facility: layout and criticalities 59

4.2.1 Liquid metal loop 60

4.2.2 Experimental set-up 61

4.2.3 Design verification 63

4.2.4 Criticalities of the facility 67

4.3 TRIEX-II facility: layout and design 67

4.3.1 Lead-lithium loop 68

4.3.2 Gas circuit 76

5 Model and results 82

5.1 0D model for TRIEX-II: mass balance of the system 82

5.2 Coupling between Simulink and COMSOL Multiphysics 85

5.3 Experimental results and analysis 87
5.3.1 Operational mode A: tests with H_2 87
5.3.2 Operational mode B: tests with D_2 95
6 Conclusions 98
Bibliography 100

List of Figures

Figure 1 - Reaction rate as function of temperature of the main fusion reactions13

Figure 2 - Deuterium-Tritium reaction 13

Figure 3 - Picture of the Joint European Torus (JET) built in the UK 16

Figure 4 – ITER vacuum chamber internals. 3D view with plasma ions 17

Figure 5 - ITER timeline from 2005 19

Figure 6 - ITER vacuum vessel 3D view. 20

Figure 7 - Cable-in-conduit conductor for ITER 21

Figure 8 - Magnet system of ITER. Toroidal field coils, poloidal field coils and the central solenoid are highlighted. 22

Figure 9 - Divertor design with components indicated 23

Figure 10 - 3D view of ITER cryostat assembled with all its penetrations. 26

Figure 11 - DEMO staged-design approach 27

Figure 12 - Tritium closed fuel cycle for a fusion reactor. The outer cycle is in red and the inner one in black 31

Figure 13 - TES schematic for the solid breeder (left) and the liquid breeder (right) 33

Figure 14 - Tritium cycle from the blanket to other systems. Red arrows indicate losses and permeation fluxes 35

Figure 15 - Hyper-Quarch layout 36

Figure 16 - Sensor pressure as a function of time in the two tests done in gas phase during Hyper-Quarch campaign 41

Figure 17 - Helical iron sensors for TRIEX-II. They are placed in a concentric way in the same measurement place 42

Figure 18 - Representation of the fluxes involved in a gas driven permeation in equilibrium mode. In dynamic mode there would not be the dissociation flux on low-pressure side 43

Figure 19 - COMSOL 2D geometry for the iron sensor simulation with a zoom of the sensor boundaries 45

Figure 20 - Simulation result for HLM734 sensor 46

Figure 21 - Simulation result for HLM735 sensor in gas phase 46

Figure 22 - Permeation sensors trend with the optimal value of the permeation parameter 48

Figure 23 - 3D view of the upper flange of the quartz chamber (left) and total assemble with steel connections (right) 49

Figure 24 - Bubble column design 53

Figure 25 - Random packing pall rings and structured packing metal sheets 53

Figure 26 - Packed column design 54

Figure 27 - Gas-Liquid interface conditions for a certain solute A 55

Figure 28 - Gas-liquid balance in a packed column 56

Figure 29 - Equilibrium and operating line 57

Figure 30 - Control system of TRIEX 59

Figure 31 - Cylindrical permeation sensor in pure Fe 62

Figure 32 - value of NTU as function of the slope of the equilibrium line. m has been varied with step of 10^{-3} 66

Figure 33 - Comparison between the computed value through the Sieverts' law and the optimal one in order to have the result Z= 80 cm 66

Figure 34 - Synoptic of TRIEX II 68

Figure 35 – Lead-lithium loop P&ID of TRIEX II 69

Figure 36 - Storage tank S100 constructive design 70

Figure 37 - Picture of S100 storage tank of TRIEX II with heating cables and all the instrumentation installed. 71

Figure 38 - Permanent magnet pump installed on TRIEX-II. 72

Figure 39 - Saturator S200 before the installation. The oxide layer is due to the heat treatment applied. 73

Figure 40 - Mellapak 452Y made of AISI steel 316L in corrugated sheets shape 74

Figure 41 - Extractor S300 constructive design 75

Figure 42 - Gas circuit P&ID of TRIEX II 77

Figure 43 - Skid A of the gas circuit 77

Figure 44 - Skid B of gas system. The vacuum pumps are positioned on the lower work plan 78

Figure 45 - ESSCO GeneSys 200D. 80

Figure 46 - Example of analogue spectrum. In this case the gas is air 81

Figure 47 - Multi tab of the software where the trend in time can be seen. The example is with air 81

Figure 48 - Simulink 0D model for TRIEX-II system balance 84

Figure 49 - Internal blocks of a subsystem of the Simulink 0D model 85

Figure 50 - Simulink S-function for the extractor 85

Figure 51 - Layout of the coupled Simulink-COMSOL models. The S-function block is highlighted with a red circle 86

Figure 52 - Permeation sensors trend for Test#1 91

Figure 53 - Permeation sensors trend for Test#5 92

Figure 54 - Concentrations trend over time across the extractor S300 93

Figure 55 - Comparison of the extraction efficiency in Test#1 between experiments and 0D model. 93

Figure 56 - Permeation fluxes through pipes, saturator and extractor 94

List of Tables

Table 1 - ITER vacuum vessel data 20

Table 2 - Key parameters of pre-concept design of DEMO 28

Table 3 - Comparison between HCLL and WCLL concepts 29

Table 4 - Tritium main parameters for ITER and DEMO 30

Table 5 - Test results on Hyper-Quarch device 38

Table 6 - Solubility, permeability and diffusivity of iron and niobium. As can be seen, solubility and permeability of niobium have opposite behaviour as function of temperature respect to iron 40

Table 7 - Helical sensor geometrical parameters 41

Table 8 – Main transport parameters 45

Table 9 - Input parameters for HLM734 and HLM735 simulations 46

Table 10 - Error calculation for the gas phase model 47

Table 11 - Operative conditions and results of TRIEX experimental campaign 63

Table 12 - TRIEX data and preliminary calculations 64

Table 13 - Design parameters of S100 of TRIEX II 70

Table 14 - Operative conditions of the pump 72

Table 15 - Operative conditions of the saturator S200 73

Table 16 - Extractor S300 operative conditions 75

Table 17 - Technical specifications of GeneSys 200D 79

Table 18 - Parameters of operational mode A 87

Table 19 - Solubility values from three different authors, evaluated at 400°C 89

Table 20 - Experimental results for the operational mode A 90

Table 21 - Experimental efficiency for the Test#1 and Test#5 evaluated with the sensors 92

Table 22 - Permeation fluxes maximum values at t=0 s. 95

Table 23 - Operating conditions for op. mode B 95

Table 24 - Tests results of operational mode B with deuterium 96

1 Introduction

The purpose of this thesis is to analyse the features of tritium extraction from lithium-lead with a packed column, that is used in liquid breeding blanket concepts for ITER and DEMO. In particular, the experimental campaign on TRIEX-II facility built in C. R. ENEA Brasimone has been followed and the results obtained have been analysed, trying to qualify the packed column configuration. Moreover, three models have been developed trying to reproduce the functioning of the permeation sensors used and to have the hydrogen mass balance of TRIEX-II system.

In Chapter 2, the physics behind fusion energy is described together with the main advantages and disadvantages respect to other energy sources. Later, the two main projects regarding nuclear fusion are analysed: ITER and DEMO. The first is under construction in Cadarache, France, and it should be operative for 2025 and demonstrate fusion feasibility. DEMO will be the first fusion reactor to generate electricity and the first kilowatt production is expected for the middle of the century. The main design concepts for these two projects are listed and analysed. In the last section, the tritium extraction process from the blanket is described together with the permeation phenomena and the related safety issues.

In Chapter 3, the permeation sensors behaviour has been analysed and the model for the gas phase driven permeation is described, together with the issues about the solubility and permeability of the materials chosen for the sensors. A comparison between the model and the results obtained with the probes gave good agreement. Moreover, the Hyper-Quarch device, installed in C. R. ENEA Brasimone, and its experimental campaign are described, with the criticalities found during the tests and why its upgrade Hyper-Quarch-II will be developed. The purposes of the new device will be a detailed qualification of the permeation sensors and a new measure of hydrogen solubility in lithium-lead.

In Chapter 4, the Gas Liquid Contactor (GLC) working principle is described with the different possible technological solutions used in industry. The packed column design is analysed more in detail with the "transfer units" method, that has been applied to the design verification of

the extraction column built for TRIEX. In the last part, the layouts of the two facilities TRIEX and TRIEX-II are described with a characterisation of the instrumentation installed.

In Chapter 5, the 0D-model developed with Matlab/Simulink interface is shown, describing the mathematical model adopted for the hydrogen mass balance in the lithium-lead loop of the facility. This model has been coupled with the 2D-model built for the extractor of TRIEX-II, using COMSOL Multiphysics software. After that, the results of the experimental campaign are shown and analysed, with the benchmark of the code. In the last part, the criticalities found during the campaign and the issues over the results are listed.

2 Fusion basics and engineering

Energy demand and consumption have continuously increased during the last century and will increase in the future, especially due to urbanization and growth of developing countries. New investments in sustainable energy sources are needed to reach environmental requirements for zero or low CO_2 emissions. Nuclear fusion could be a valid source of secure, clean and safe energy [1] [2].

2.1 Physical process

Nuclear fusion is the physical process that occurs inside the stars. Differently from nuclear fission, where one heavy atom is split in two thanks to a neutron, in fusion two light atoms combine together at very high temperatures and pressures (inside the Sun there are about 15 million °C and high pressures due to gravitational forces) and the result is a nucleus of a different element and a strong release of energy, due to the mass difference between reactants and products. At these temperatures, every gas become plasma, the fourth state of matter, where electrons are completely detached from the positive nucleus made of protons and neutrons. Plasma is a sort of charged gas where ions (positive charge) and electrons (negative charge) are physically separated [1].

To reproduce this phenomenon on Earth, gases must reach even higher temperatures than the Sun core (about 150 million °C) in order to have completely ionised atoms. The simplest reaction to achieve is the one with two isotopes of hydrogen, deuterium (^2H) and tritium (^3H), often indicated with D and T respectively. This reaction is the one with the highest fusion reaction rate at temperatures around 10^6 °C (see Figure 1).

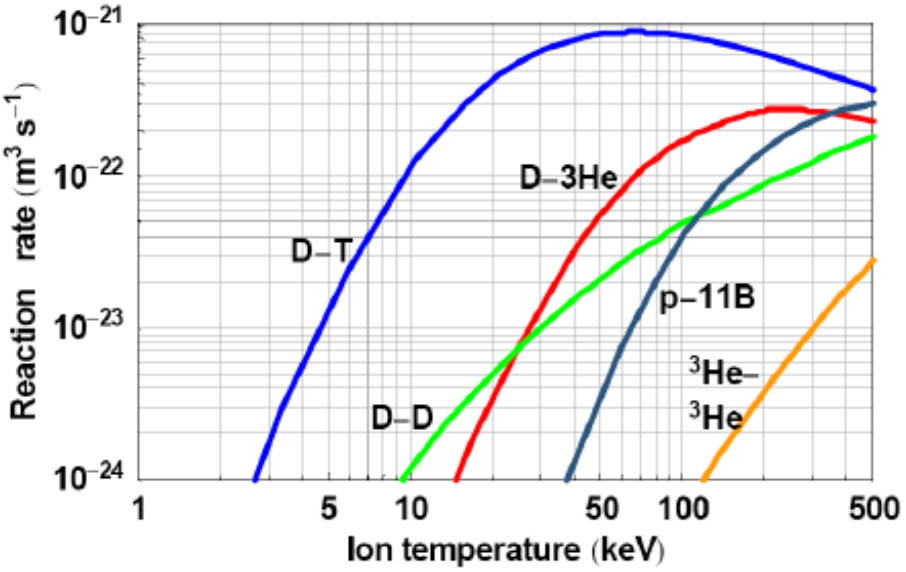

Figure 1 - Reaction rate as function of temperature of the main fusion reactions [3].

Other possible reactions are D-D and D-^{3}He, but they have more severe requirements: temperatures of one or more order of magnitude higher and ^{3}He is almost absent on Earth. Another possible fusion reaction could be the one between a neutron and an atom of deuterium that would involve a lighter element as the neutron, but in this case the self-sustainability disappears because *n* is required as a source [1].

The product of the combination D-T is an α particle (nucleus of a He atom, 2 protons and 2 neutrons) and a fast neutron (see Figure 2).

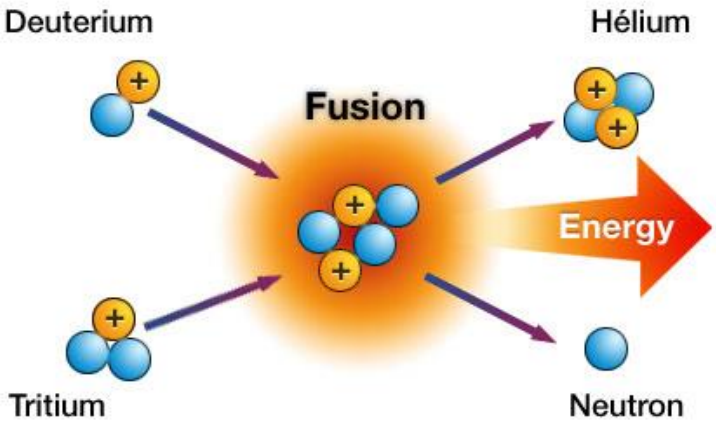

Figure 2 - Deuterium-Tritium reaction [4].

One of the positive aspects is that one of the two reactants is plentiful. Deuterium is present in heavy water D_2O, part of natural water with a

fraction of 1 over 6000 so it is virtually inexhaustible. Tritium, instead, is a radioactive isotope of hydrogen with a half-life of about 12 years. Naturally, it is produced in the atmosphere from the collision of air molecule with cosmic rays and it is found in very small traces in groundwater [5]. For this reason, it must be produced *in situ*. It can be produced from neutron bombardment of lithium, that is quite abundant in Earth's crust and oceans. Two possible reactions are possible.

$$Li^6 + n(slow) \rightarrow \alpha + T + 4.8\ \text{MeV}$$

$$Li^7 + n(fast) \rightarrow \alpha + T + n - 2.5\ \text{MeV}$$

The first reaction produces energy and the second requires energy. Li^7 is more abundant (92.6%) but the reaction with Li^6 (7.4%) is the easiest to initiate, so it is easier to have an energy release in tritium breeding. Moreover, fuel consumption is much lower than in other reactors: a 1 GW_e power reactor should consume about 100 kg of fuel each year [2].

In energy terms, fusion reactions are significantly more energetic than chemical reactions. D-T reaction produces 17.6 MeV in the form of kinetic energy of the product particles (14.1 MeV for the neutron and 3.5 MeV for the α particle). The energy amount can be computed from the mass difference of reactants and products thanks to the formula $\Delta E = \Delta m \cdot c^2$.

$$^2_1H + ^3_1H \rightarrow\ ^4_2He + n$$

c^2 is a very large number, so a small amount of missing mass determines a high value of energy released. The ionisation energy of hydrogen is 13.6 eV [2], less than one-millionth of fusion energy. To compare with common fuels, the combustion of a molecule of methane CH_4 release an energy of 8.3 eV (computed with the PCI of methane, 50 MJ/kg), very much lower. The energy distribution among the products depends inversely on the mass of the particles. The ratio between the α particle and the neutron is equal 4, so the energy partition becomes 4/5 for the neutron and 1/5 for the He nucleus, that explains the 14.1 and 3.5 MeV cited before.

Another positive aspect of fusion is about the second side of the reaction. In nuclear fission one of the principal issues is related to radioactive waste produced during the operation of the reactor. They are difficult to manage

and must be treated carefully for many years after the decommissioning of the plant. In the D-T fusion reaction, the only products are the α particle and the neutron. The first is used to maintain the high temperature of the plasma itself, for auto-sustainment, and the second will be used for electricity production. Neither of the two particles has radioactive problems and that is why nuclear fusion can be considered an almost complete clean energy source. The main radioactivity issues regard tritium handling and the activation of materials of the reactor due to neutron bombardment [1].

Fusion is also intrinsically safe. Differently from fission, neutron appears only in the product side of the reaction so there is not the concept of criticality and chain reaction that can lead to a divergence of the power produced. Moreover, in the case of malfunctioning that cannot maintain the fuel replenishment, the plasma will cool because the reaction itself keeps the temperatures high enough to sustain the fusion reaction. Without this one, the temperature decreases very fast until the complete shutdown [1].

2.2 ITER and DEMO projects

To exploit the nuclear fusion process potential, a suitable way to produce electricity from the reaction is needed. One of the most promising is the tokamak configuration. This machine uses magnetic fields to confine and shape the plasma avoiding that it meets with the walls. There are two major projects that are based on tokamak machines: ITER and DEMO. The first is under construction in Cadarache, France, and it will demonstrate the feasibility of a fusion reactor trying to obtain a net energy production. ITER first plasma will be in 2025. DEMO, instead, it still in a pre-conceptual design phase and it will be ITER successor. It will produce electricity from fusion reaction in order to come closer to a possible future commercial fusion power plant. DEMO perspectives are quite far in the future, expecting a possible first electricity production around the middle of the century [6] [7].

2.2.1 Tokamak device

The tokamak is a machine to confine plasma thanks to magnetic fields. The first was developed in the '60s in the Soviet Union and then adopted as the most promising technology to confine the plasma and achieve fusion reaction. The actual world's largest tokamak is JET, visible in Figure 3 [8].

Figure 3 - Picture of the Joint European Torus (JET) built in the UK [8].

The characteristic of a tokamak device is the particular shape of its vacuum chamber, similar to a doughnut. The D-shape has the advantage to reduce the net force on the internal edge of the reactor. Towards the centre, the force is higher due to the higher magnetic field, so that the flatter edge supports better the net force on it [9]. Inside, the vacuum is continuously kept through external pumps, necessary condition to reach the formation of plasma. After decontamination of the chamber from all impurities, the fuel can be introduced and then heated up thanks to a strong current that runs through it. To guarantee the stability and the confinement, strong magnetic fields are created thanks to different magnetic coils: poloidal and toroidal field coils [8]. The more massive toroidal coils create a magnetic field in poloidal direction that has the function to confine the plasma. Poloidal coils, instead, create a magnetic field in vertical direction that guarantees the stability of the plasma, avoiding as much as possible the contact between very high temperature charged particles and the walls. The third main magnetic component is the central solenoid, the one in charge to heat up the

plasma. The solenoid works as the primary winding of a transformer and, thanks to Faraday's law, induces a current in toroidal direction in the plasma particles, that work as the secondary winding. In a tokamak can be installed also some correction coils, that have the function to compensate field errors caused by geometrical deviations or other possible perturbations to the magnetic fields [8].

2.2.2 ITER

The International Thermonuclear Experimental Reactor, simply known as ITER, will be the first fusion reactor with net energy production. 35 nations are collaborating to build it and it will be the world's largest tokamak, about ten times the largest machine operating at present days. The future internals of ITER tokamak are shown in Figure 4. It will prove the feasibility of fusion on a large scale and a carbon-free source of energy. ITER will be the first device to maintain the fusion reaction for long periods and will be built to investigate technologies, materials and physics regimes necessary to the production of electrical energy, even if it will never produce electricity [6].

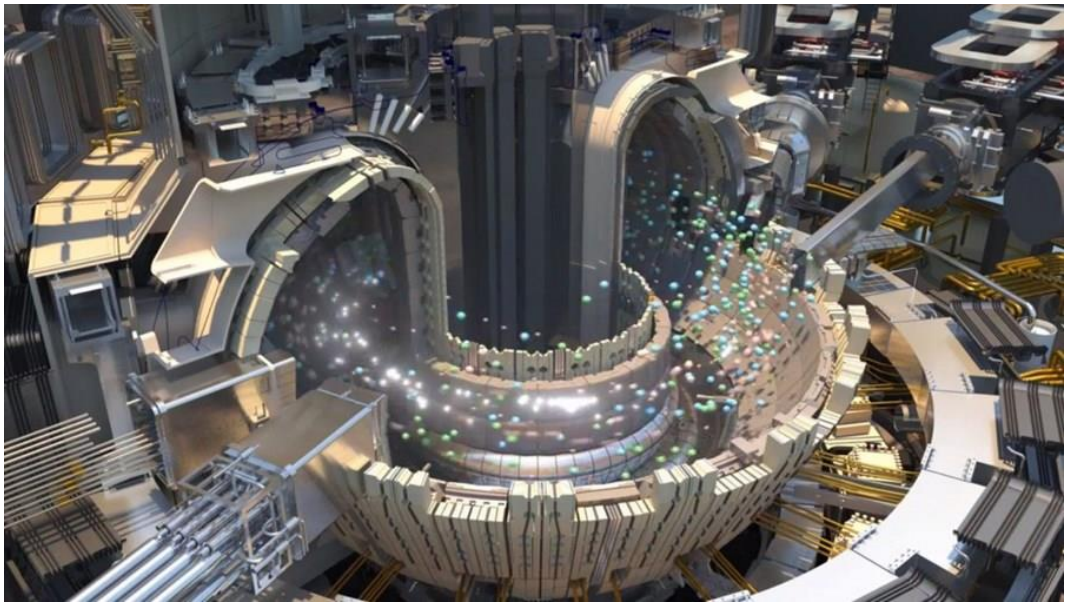

Figure 4 – ITER vacuum chamber internals. 3D view with plasma ions [6].

The main goals of ITER are [6]:

- *Net energy production with 500 MWth output power*
  The actual record is held by JET, the world's largest tokamak, with 16 MWth and an input of 24 MW. The goal of ITER is to reach $Q \geq 10$ with an input power of only 50 MW.

- *Integrate operation of new technologies*
  The scale-up of ITER is huge. It will demonstrate the feasibility of fusion closer to the size of a real power plant than today's experimental fusion technologies and devices. This will be a test of multiple aspects that will be used in a future commercial power plant.

- *Self-sustaining deuterium-tritium reaction achievement*
  One of the goals of fusion is to reach the self-sustainment of the fusion reaction for long periods of time. ITER will produce much more energy and scientists are confident that the plasma will remain stable for long periods. Stability of the plasma is one of the key aspects to reach the self-sustainment of the reaction, that is needed to achieve the net energy production.

- *Test tritium production*
  Tritium will be produced *in situ* because of its fast radioactive decay. ITER will test the feasibility and the efficiency of tritium breeding inside the vacuum vessel together with its removal. It will be a unique opportunity to test mock-up of breeding blankets in a real fusion environment.

- *Demonstrate the safety of a fusion plant*
  ITER has been recognized as a nuclear plant and so it is examined with the rigorousness and impartial way applied in the nuclear field. One of the goals of this device is to demonstrate the safety of fusion reaction and plant, with secure control of the plasma and negligible consequences for the environment.

In Figure 5, the timeline schedule of ITER can be seen. The first plasma is expected in 2025 and after ten years the operations with deuterium and tritium will begin.

ITER Timeline

2005	Decision to site the project in France
2006	Signature of the ITER Agreement
2007	Formal creation of the ITER Organization
2007-2009	Land clearing and levelling
2010-2014	Ground support structure and seismic **foundations** for the Tokamak
2012	Nuclear licensing milestone: ITER becomes a Basic Nuclear Installation under French law
2014-2021	Construction of the Tokamak Building (access for assembly activities in 2019)
2010-2021	Construction of the ITER plant and auxiliary buildings for First Plasma
2008-2021	Manufacturing of principal First Plasma components
2015-2023	Largest components are transported along the ITER Itinerary
2020-2025	Main assembly phase I
2022	Torus completion
2024	Cryostat closure
2024-2025	Integrated commissioning phase (commissioning by system starts several years earlier)
Dec 2025	**First Plasma**
2026	Begin installation of in-vessel components
2035	**Deuterium-Tritium Operation begins**

Figure 5 - ITER timeline from 2005 [6].

ITER will be the top among tokamak devices and a great technological challenge to win. Its principal components are described in the next subsections.

Vacuum vessel

The vacuum vessel (VV) is a giant hermetically sealed steel container where the plasma can flow continuously in a circle inside the doughnut-shaped chamber. This vessel represents the first containment barrier for leakages and radioactivity and the first heat removal system. It consists of a double wall protection and an in-wall shielding. Between the double walls, water circulation is used to cool down the vessel. The structure of the vessel will provide mechanical support to in-vessel components such as the blanket and the divertor [10].

Forty-four ports will allow access for instrumentations for remote handling, diagnostics, vacuum and heating. For example, five lower ports will be used

to substitute the divertor cassette when exhausted and other four are connected to the vacuum pumping system.

The vacuum vessel is enclosed in a bigger vacuum chamber called cryostat, where also the entire magnet system is enclosed in. ITER vacuum vessel data are shown in Table 1.

Table 1 - ITER vacuum vessel data [10].

Parameter	**Value**	**U.o.M.**
Internal total volume	1400	[m^3]
Plasma volume	840	[m^3]
Outer diameter	19.4	[m]
Height	11.4	[m]
VV weight	5200	[t]
VV weight with blanket and divertor installed	8500	[t]

In Figure 6, the vacuum chamber with VV highlighted can be seen.

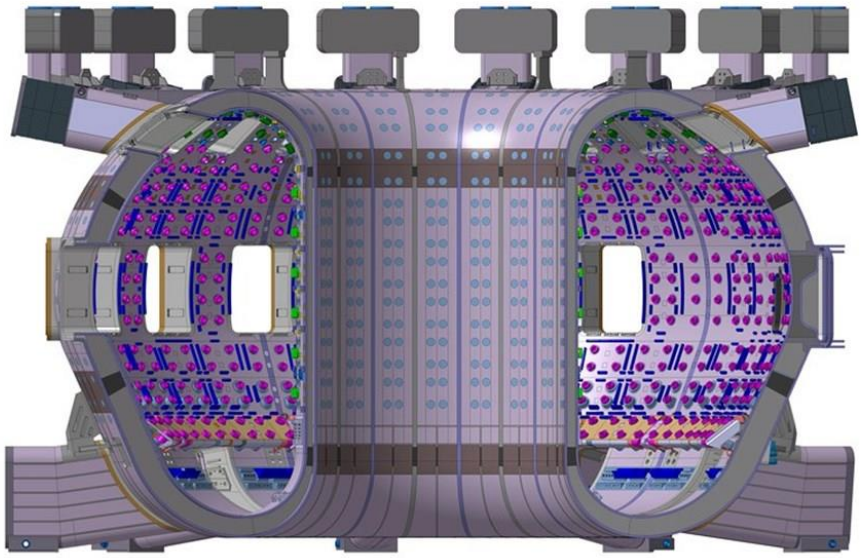

Figure 6 - ITER vacuum vessel 3D view [11].

Magnet system

The magnet system will be made in superconducting material to avoid the high electrical resistance of normal conductors, that will lead to too high heat production due to very elevated currents inside the magnets. The materials chosen are Nb3-Sn and Nb-Ti that become superconductive when cooled with liquid helium at 4 K. The "cable-in-conduit conductor" for ITER can be seen in Figure 7.

Figure 7 - Cable-in-conduit conductor for ITER [12].

Superconducting strands are mixed with copper and closed together in a steel jacket, that has also structure function. These cables are divided into the four subsystems of the magnet system [12]:

- *Toroidal field coils*: there will be eighteen segments of toroidal magnets placed around the centre. They are among the biggest component of ITER with their 9x17 m^2 dimension. The maximum field produced will be about 11.8 T.

- *Poloidal field coils*: there will be six superconductive rings placed outside the toroidal field coils system and will produce a maximum of 6 T. This has the function of shaping and stability of the plasma keeping it away from the walls. The larger of the ring will have a diameter of 24 meters.

- *Central solenoid*: the central solenoid induces a strong current of 15 MA in the plasma for durations of 300-500 seconds. It is the most powerful

magnet of ITER with a 13 T field produced in the centre. The central solenoid will be strongly supported by external structures in order to resist the strong electromagnetic forces that pull in different directions.

- *Correction coils*: eighteen corrective coils will be placed between the toroidal and poloidal coils systems. Their function is to compensate for possible field errors caused by geometrical deviations that occur with assembly and manufacturing tolerances. They are smaller and lighter than other magnets and a lower current run through them.

Other important systems are the *magnetic feeders*, that connect the magnets to their power supply and distribute the cryogenic liquid, and two *non-superconducting coils* inside the vacuum vessel to improve control capabilities. In Figure 8, a view of the future magnets installed in the vacuum chamber of ITER is shown.

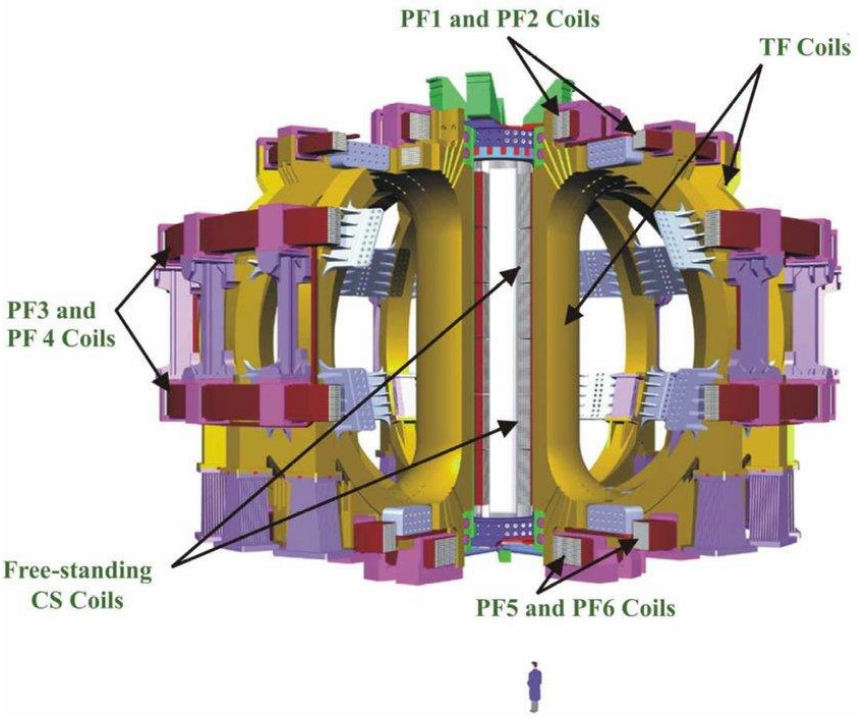

Figure 8 - Magnet system of ITER. Toroidal field coils, poloidal field coils and the central solenoid are highlighted [13].

Divertor

The divertor has the main functions to extract the heat and to remove ashes produced with fusion reaction. Moreover, it protects the surrounding walls from neutronic loads and has also the function to minimize plasma contamination that could lead to a cool down. There will be fifty-four cassette assembles in the lower part of the vacuum vessel made of three components that will face the plasma: inner and outer vertical targets and the dome. The two vertical targets are placed at the intersection of magnetic lines, so they will be strongly bombarded by fast particles and must resist to very high heat loads. The dome must also avoid that ashes and contaminating particles leave the lower zone of the vessel and reach the plasma. The material chosen for the divertor is tungsten, the metal with the highest melting point. The heat loads that divertor must withstand have been estimated to be around $10\ MW/m^2$ in steady-state operation and $20\ MW/m^2$ during slow transients [14]. In Figure 9, the design of the divertor that will be installed in ITER is reported.

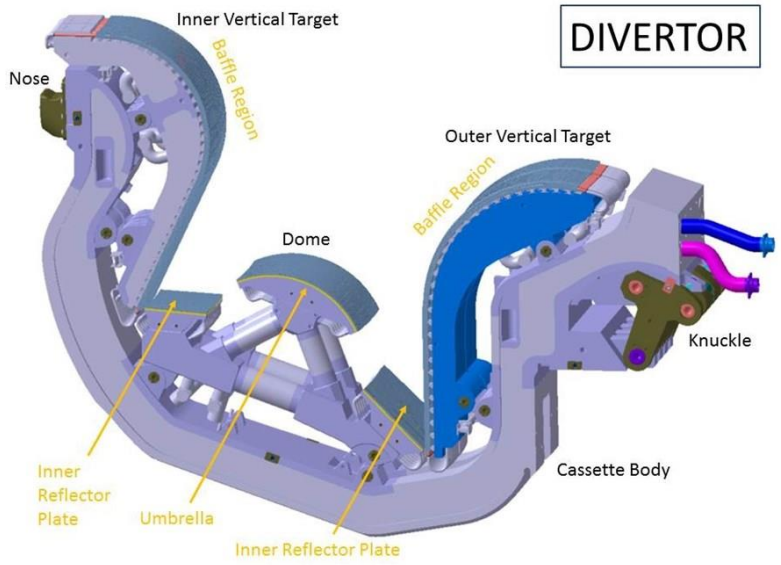

Figure 9 - Divertor design with components indicated [15].

Blanket

The blanket has the function to protect the vacuum vessel and the magnets from the high heat and fast neutrons produced from the fusion

reaction. The part that faces directly the plasma is the first wall, composed by detachable panels made of beryllium tiles bonded with a copper alloy and stainless steel. Beryllium has been chosen because of the low plasma contamination and low fuel retention requirements [16]. These panels will be cooled with water and in these years two kind of them have been qualified in order to resist to a heat flux of 2 MW/m^2 and 4.7 MW/m^2. The outer part of the blanket slows down the neutron coming from the centre and is cooled by water, but in a future real power plan, this energy will be used to produce electricity. In later stages of operation of ITER, some modules of the blanket will be replaced with specialized ones to test tritium breeding, essential feature to have the replenishment of fuel for fusion [16]. In 2017 six different concepts were planned to be tested and are here briefly described:

- *HCLL TBS*: Helium Cooled Lithium Lead, proposed by the EU. This system uses lithium-lead PbLi as tritium breeder and neutron multiplier and the coolant is helium, that flow at 8 MPa and inlet/outlet temperature of 300/500 °C. The liquid metal is enriched with ^6Li. After fuel breeding, the PbLi goes to the tritium removal system that will manage the tritium produced. The structure temperature, made in Eurofer, ranges between 350 and 550 °C [17].
- *HCPB TBS*: Helium Cooled Pebble Bed, proposed by EU. This configuration uses Li_4SiO_4 or Li_2TiO_3 pebble beds as breeder and beryllium pebble beds as neutron multiplier. Coolant is helium in the same condition of the HCLL system. The maximum temperatures reached are 920 °C for ceramic, 650 °C in beryllium and 550 °C in Eurofer structure [17].
- *WCCB TBS*: Water Cooled Ceramic Breeder, proposed by Japan. This system uses Li_2TiO_3 as ceramic breeder and water as a coolant. The breeder is beryllium in pebbled beds form. The maximum temperatures are 900 °C for the ceramic, 600 °C in beryllium and coolant is pressurized with inlet/outlet temperature of 280/325 °C. This configuration is similar to HCPB except for the choice of the coolant [17].
- *HCCR TBS*: Helium Cooled Ceramic Reflector, proposed by Korea. It has Li_2TiO_3 pebble bed as breeder, beryllium pebbles as a multiplier and

RAFM steel has been chosen as structure material. Moreover, graphite is present as a reflector in order to recover and shield from neutrons that escape. Coolant is helium with inlet/outlet temperatures of 300/500 °C [18].

- *HCCB TBS*: Helium Cooled Ceramic Breeder, proposed by China. Uses Li_4SiO_4 pebble beds as a breeder, beryllium as multiplier and helium as a coolant. The structural material is RAFM steel. The maximum temperatures are 900 °C in the ceramic, 600 °C in beryllium and 550 °C in the steel [17].
- *LLCB TBS*: Lithium Lead Ceramic Breeder, proposed by India, has both solid and liquid breeder. It uses Li_2TiO_3 pebble beds as the solid breeder and PbLi as the liquid one. The structural material is RAFM steel. There are two coolants, helium for FW panels and PbLi for the ceramic breeder. PbLi acts also as neutron multiplier. Inlet/outlet temperatures of lithium lead coolant are 300/480 °C [17].

In 2018, the HCLL concept has been substituted with the WCLL, where water is used as coolant. In 2019, the HCCR and LLCB configurations have been discarded, so that only four different TBMs will be tested in ITER.

Cryostat

The ITER cryostat will be the largest steel vacuum chamber ever built with his total volume of 16000 m^3 and it will contain the superconducting magnets and the vacuum vessel. It is almost 30 meters wide in its largest section. The cryostat has 23 penetrations for maintenance operations and more than 200 for cooling systems, magnet feeders, auxiliary heating, diagnostics and replacement for blanket and divertor sections. The entire structure will have to maintain a vacuum pressure of 10^{-4} Pa, a very restrictive requirement for such a large chamber [19]. A 3D view of the cryostat is shown in Figure 10.

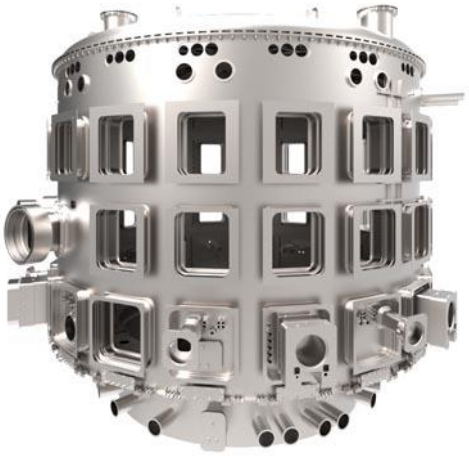

Figure 10 - 3D view of ITER cryostat assembled with all its penetrations [19].

2.2.3 DEMO

ITER will be the first big step towards the demonstration of the feasibility of fusion and its applications. The second major step will be DEMO, DEMOnstration Fusion Reactor, that will jump closer to the design of a real nuclear fusion power plant with production of electricity. Europe started in 2014 a comprehensive design study of DEMO with the aim to produce several MWs of electric power around the middle of the century. The revisited ITER schedule has necessitated a review of DEMO development strategy and schedule, considering that, where possible, DEMO will exploit ITER results. Although, the revised schedule maintains as target the production of electricity for the middle of the century. Another issue is the low tritium supply. DEMO will have a closed tritium fuel cycle, but to have an efficient tritium production the tritium breeding system will have to have the maximum possible performances, considering the experience and results of ITER later years of operation. DEMO will be the "test facility" for a real breeding blanket. It must be used to test and validate more advanced breeding blanket concepts, that can have the potential to be installed in a first fusion power plant. In synthesis, the revised schedule for DEMO consists of three main phases [20]:

- Pre-Concept Design Phase to explore some DEMO concepts and create a list of system requirements up to 2020.
- Conceptual Design Phase to validate the baseline concept up to 2027.
- Engineering Design Phase to develop a detailed design. It should begin around 2030.

In Figure 11, the roadmap of these three design steps can be seen.

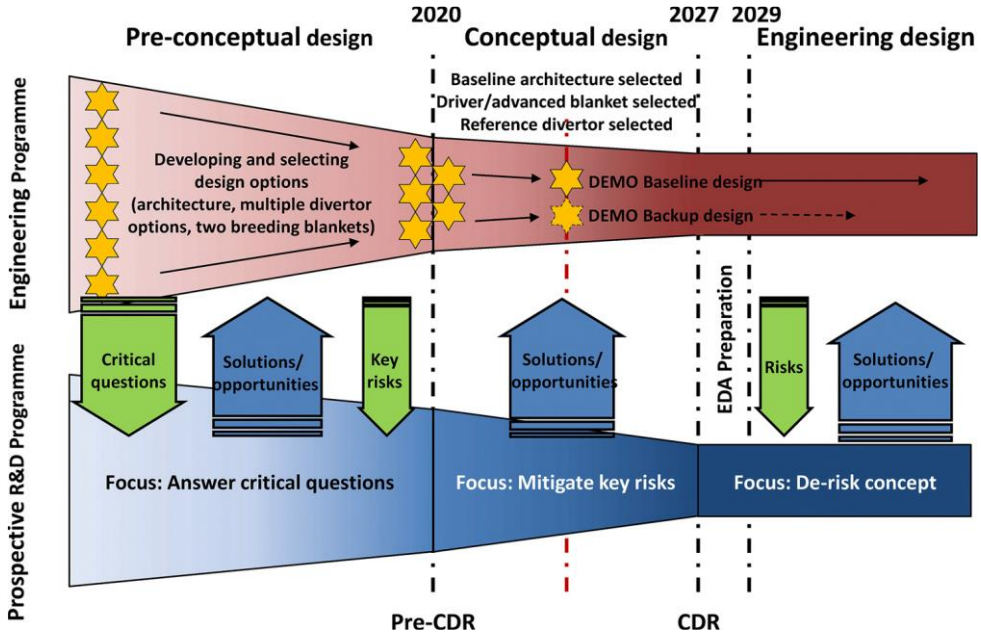

Figure 11 - DEMO staged-design approach [20].

A pillar of the PPPT (Power Plant Physics and Technology) DEMO design is the establishment of a baseline architecture that can integrate all the sub-systems of the plant. Work in progress continues to focus on the design integration of a pulsed baseline DEMO plant, but alternative configurations are under investigation to understand their relevance. In this early design phase, three main criteria have been used to set a minimum tokamak size: divertor protection, access to High-confinement mode and the maximum field in the conductor of TF coils with their design. The divertor power handling has been discovered as a very important size-driver for DEMO [20]. In Table 2, the main characteristics and parameter of actual concept design of DEMO are shown.

Table 2 - Key parameters of pre-concept design of DEMO [20].

Parameter	Value	U.o.M.
Major radius	9	[m]
Aspect ratio	3.1	
Plasma current	18	[MA]
Toroidal field peak	> 12.5	[T]
Auxiliary heating power	50	[MW]
Fusion power	2000	[MW]
Net electricity production	500	[MW]
Burn time	7200	[s]
Down time	< 600	[s]
Average electron density	$0.73*10^{20}$	$[m^{-3}]$
Neutron wall loading	1.04	$[MW/m^2]$

Some assumptions have been made for these design characteristics and they are summarized in the next points [20]:

- Single-null divertor cooled by water made in tungsten;
- Low-temperature superconducting magnets in Nb_3Sn;
- Max value of magnetic field around 12 T;
- Thermal conversion efficiency > 30 %;
- Self-sufficient tritium fuel cycle;
- Blanket lifetime: around 20 dpa for the starting blanket and 50 dpa for the second one;
- DEMO plant lifetime around 7-8 fpy (full-power years)

Multiple studies have been carried out to obtain these design features and main assumptions, especially sensitivity analyses on different parameters that change plant performances and operations.

In the following part, main recent achievements in DEMO design will be summarized, regarding some main aspects and components of the plant [20].

- *Breeding blanket*: DEMO will act as "Component Test Facility" for the breeding blanket. At the moment, there are four design options, with different design level, that are considered as potential driver blankets. These configurations use helium, water and PbLi as coolants and a solid ceramic or liquid PbLi as tritium breeder and neutron multiplier. There are also studies about the choice of materials to withstand the strong

irradiation coming from the centre of the tokamak. Experience from fission power plants materials is exploited and new dedicated facilities, such as IFMIF in Japan, are built to simulate the irradiation that will occur in DEMO reactor.

- *Balance of plant (BOP)*: there are ongoing works to assess the design and technological problems related to the Primary Heat Transfer System (PHTS) for the breeding blanket. Nowadays, two options are considered: He at 80 bar with inlet/outlet temperature 300/500 °C and water at 150 bar with 292/328 °C. These two coolants have been investigated respectively for HCLL and WCLL configurations (Table 3). Because of the pulsed nature of the reactor, an Intermediate Heat Transfer System (IHTS) equipped with an Energy Storage System is being investigated. This system should help to mitigate the pulsation effects on the power generation system.

Table 3 - Comparison between HCLL and WCLL concepts. In 2019, the WCLL has been chosen as the reference concept for liquid breeding blanket [20] [21] [22].

Issue	**HCLL**	**WCLL**
Coolant inlet/outlet temperature [°C]	300/500	292/328
Coolant pressure [bar]	80	155
Structural material	EUROFER97	EUROFER97
Coolant system	2 independent inlet and outlet manifolds for FW and BZ cooling in counter-current	2 independent systems, one for FW and one for the BZ
Total pumping power [MW]	100	17.7

- *Divertor*: eight different divertor design concepts have been developed, all with water cooling except that uses helium. Between them is included the divertor tungsten system, similar to the one that will be used in ITER and some advanced concepts with new materials and non-conventional schematics. The mock-ups are being tested with cold and hot water in order to resist to high heat fluxes. Five of them withstood at least 100 cycles at 20 MW/m^2 while the others are in production or test phase.

- *Tritium system*: design of DEMO Tritium System is developed keeping into account some main principles; application of direct internal recycling that leads to the configuration of two continuous re-cycle loops in addition to an outer one for isotopes separation and exhaust purposes. Minimisation of tritium inventory without intermediate storage and immediate use of tritium produced in breeding blanket. Environmental protection and dose minimisation in operating and accidental conditions.

- *Vacuum system*: one main activity is the commissioning of the mechanical pump train at JET in UK, with DT campaign in 2018-2020. Another activity is the development of a first complete metal foil pump module with the characterisation of the metal foil itself.

2.3 Tritium technologies: extraction from breeding blanket and permeation phenomena

Tritium extraction is a key aspect for the fuel cycle of a fusion reactor and for safety reasons. Tritium must be recovered from the breeder in an efficient way to keep to the minimum the inventory in the blanket. It must be also recovered from the plasma chamber because only 1% of tritium is burnt during the reaction, the other fraction must be recycled and get ready for re-use [23]. Moreover, ITER reactor will work with the tritium produced by CANDU reactor during their operation, but DEMO will consume bigger quantities of the hydrogen isotope because of five times thermal power expected. In Table 4, a comparison between ITER and DEMO tritium key parameters is shown [23] [24] [25].

Table 4 - Tritium main parameters for ITER and DEMO.

Parameter [U.o.M.]	**ITER**	**DEMO.**
Fusion power [MW]	500	2700
T consumption, full power day [g/d]	76	412
T production, full power day [g/d]	< 0.4	~450
T burn-up fraction [%]	3	> 2
T fuelling rate [kg/h]	1.1	~1
He flow rate in TES [Nm^3/h]	8-40	~10000
He flow rate in CPS [Nm^3/h]	75	~50000

Tritium is highly transportable and it is able to permeate through metallic barriers. Moreover, it is very reactive from a chemical point of view because it is an isotope of hydrogen. It is a beta-emitter, so particles emitted are shielded by the skin of the human body, but it is very dangerous if inhaled or ingested. For conservative purposes in the calculation of dose for workers, tritium is often considered as HTO or T_2O (where the standard protium isotope is substituted in the water molecule by T), that are more radiotoxic than gaseous form T_2 or HT. For these reasons, especially the part regarding the blanket, the human interactions must be included in every step of the design phase [23].

In DEMO there will be a closed tritium fuel cycle, divided in the inner and outer parts. The inner part includes the fuelling system, vacuum pumping system and tritium plant system. The outer part includes the breeding blanket and Tritium Extraction and Removal system. There is also a Coolant Purification System (CPS) because it is impossible to avoid contamination of coolant with tritium and there is the necessity to clean it as much as possible. In the outer fuel cycle, tritium will be present in a small fraction, some ppm, in large flows of helium. This feature will increase the difficulty to extract tritium from the stripping gas [23]. A schematic representation of inner and outer cycles is shown in Figure 12.

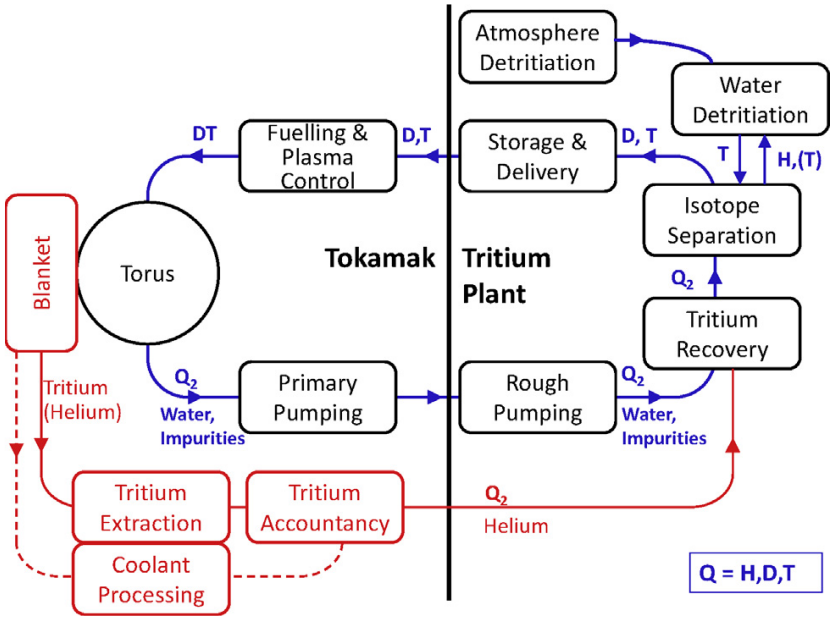

Figure 12 - Tritium closed fuel cycle for a fusion reactor. The outer cycle is in red and the inner one in black [23].

Based on the state of the breeder, tritium extraction techniques are different. Basically, there are two kinds of breeder: solid and liquid. The first comprehend multiple types of lithiated ceramic. For the liquid option, the main candidate is the lead alloy Pb15.7Li (melting point 235 °C). In both cases, tritium permeation into the coolant is an issue to be faced, because it could be released into the atmosphere if not properly removed. Moreover, tritium removal should occur mainly into the TER system in order to reduce as much as possible its recovery in the CPS [18].

In ITER reactor the first step to remove tritium from the breeder is using a purge gas and helium is the reference choice, because is an inert gas and there are no risks of chemical reactions. In the solid breeder configuration, it is fluxed directly through the ceramic pebble beds breeder inside the blanket. With liquid breeder, the advantage is that is possible to not remove directly tritium in the blanket but take the lithium-lead to a dedicated system outside. The reference technology for ITER is the Gas Liquid Contactor - packed column, but also the Permeation Against Vacuum (PAV) concept is considered as an option [18]. Another difference between the two types of breeder is the type of molecule to remove. In solid breeder, there will be Q_2 and Q_2O molecules while in lithium lead tritium will be extracted in the form Q_2 only (where Q identifies a hydrogen isotope). Q_2 can be extracted with gas liquid contactor while Q_2O will be removed thanks to adsorption columns [23]. Different methods have been proposed to remove the tritium from the purging gas, such as cryogenic trap, cryogenic adsorption, getters, permeators and catalytic membrane reactors [26] [27]. In Figure 13, it is possible to see a concept for the TER with the two types of the breeder.

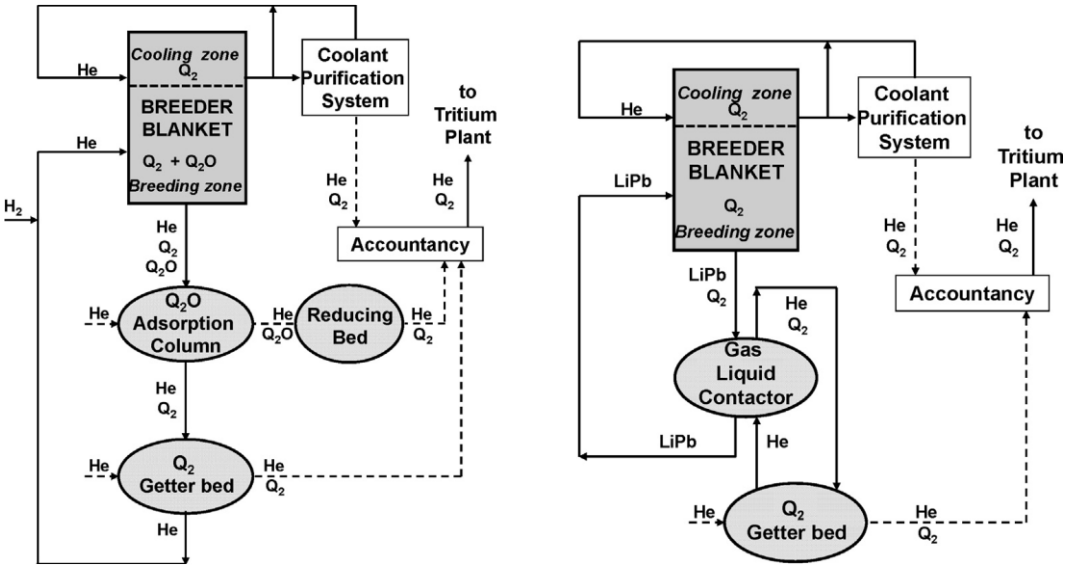

Figure 13 - TES schematic for the solid breeder (left) and the liquid breeder (right) [23].

Whatever the chosen processes, in the TER two components in parallel will have to operate together: the first will remove tritium from helium while the other will be regenerated. This is necessary to always have an extraction system free from tritium accumulated during the previous cycle of operation. In this way is possible to achieve a continuous T removal from the blanket, but this cyclic mode of operation can cause fluctuation in tritium flow rates and concentrations [23]. Another issue to consider is the permeation of tritium through the pipes to other components, such as the walls of lines inside the port cell where the TER will be connected to the blanket. In ITER this effect is easier to deal with, because of low tritium inventory. Instead, in DEMO, tritium is produced in much bigger quantities (Table 4) because of the higher energy produced, that means to a stronger neutron flux that hit the walls and the breeding zone. Moreover, more safety precautions relative to permeation phenomena must be considered [23].

An important issue for the liquid blanket concept is the solubility of tritium in PbLi. The values of Sieverts' constant for hydrogen in lithium lead reported in literature are spread over four orders of magnitude, but different experimental modes and material used could explain such a wide scattering of the results [28]. The solubility gives the amount of tritium accumulated in PbLi and the equilibrium partial pressure: with a higher solubility is higher the quantity dissolved in lithium-lead, but it is lower the

equilibrium partial pressure. Vice versa, a lower solubility means a higher equilibrium partial pressure and lower quantity of tritium accumulated in PbLi. The problem is that a higher partial pressure leads to higher permeation fluxes through the components because it depends on the high-pressure side of tritium (sections 3.2 and 3.3).

For solid breeder concepts, one of the main problems is the permeation of tritium to the coolant. Tritium must be removed by the Helium Coolant System (HCS) with an appropriate CPS to minimize quantities that could permeate in the steam generator, where coolant from the primary loop comes close to the one of the secondary loop, that will go to turbine system. In ITER a copper oxide layer, PTSA and a getter will be installed as CPS. In this way, the hydrogen in the coolant will oxidize and will be removed through a three stages process [29]. With this method, a higher radiological risk must be considered because of the formation of Q_2O molecules. For DEMO, additional studies and design must be done to achieve a good CPS because of the big quantities of tritium to manage respect to ITER. If water will be chosen as coolant, it will be necessary a very efficient detritiation system to reduce as much as possible the tritium released into the environment: in the case of DEMO, the maximum value of tritium released in the environment is considered to be 1 g per year that become only 25 mg per day. Consequently, to achieve this goal not only an efficient CPS will be needed but also permeation barriers [23]. In Figure 14 a scheme of the tritium cycle is shown.

In the case of the WCLL TBS tritium permeate from Pb15.7Li loop to water coolant and generate HTO. Two strategies can be adopted to remove tritium from water: storage water inside a dedicated tank until than tritium decay and water can be reintroduce inside the system or use a Water Detriation System, which is very complex and expensive. The main object is to minimise the tritium permeated inside water coolant.

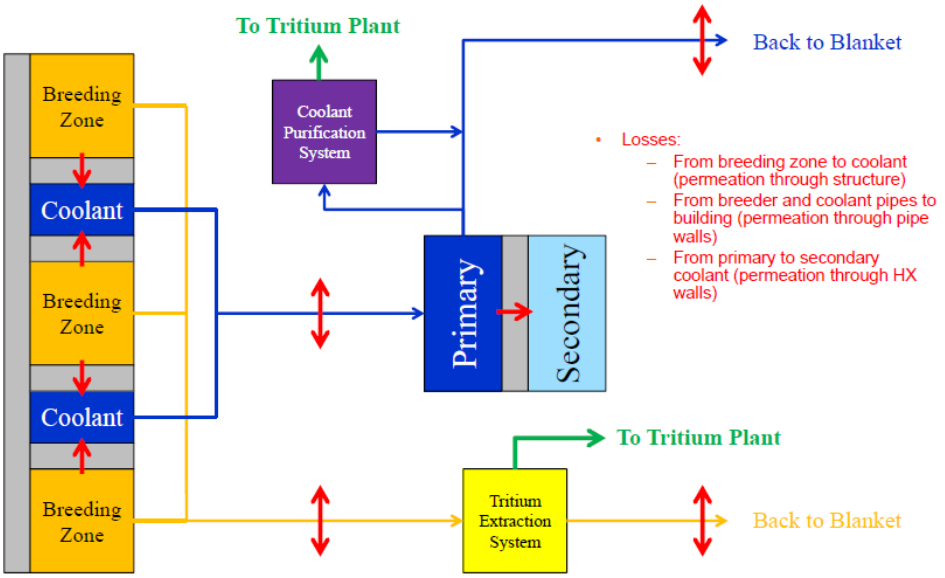

Figure 14 - Tritium cycle from the blanket to other systems. Red arrows indicate losses and permeation fluxes [30].

3 Hyper-Quarch

Tritium permeation is a phenomenon to keep into account from the point of view of safety and for the evaluation of inventories and losses in order to guarantee the fuel self-sufficiency. In order to do that, a suitable sensor must be developed to measure tritium concentration in the different steps of its cycle, from the breeding to its management in tritium processing systems. For these purposes, at ENEA C. R. Brasimone, two advanced permeation sensors have been developed to measure the concentration of hydrogen isotopes in PbLi; they have been tested in a suitable lab-scale device called Hydrogen Permeation Quartz Chamber (Hyper-Quarch) [31].

3.1 Hyper-Quarch: layout and results

The developed device has been built thinking to possible leakages of hydrogen to the environment and trying to have the highest vacuum degree and clean conditions in the circuit, in order to avoid as much as possible contaminations. The two types of iron sensors, cylindrical and helical-shaped, have been tested in equilibrium mode (see 3.2 section for detailed description of the sensors). The layout of the device can be seen in Figure 15.

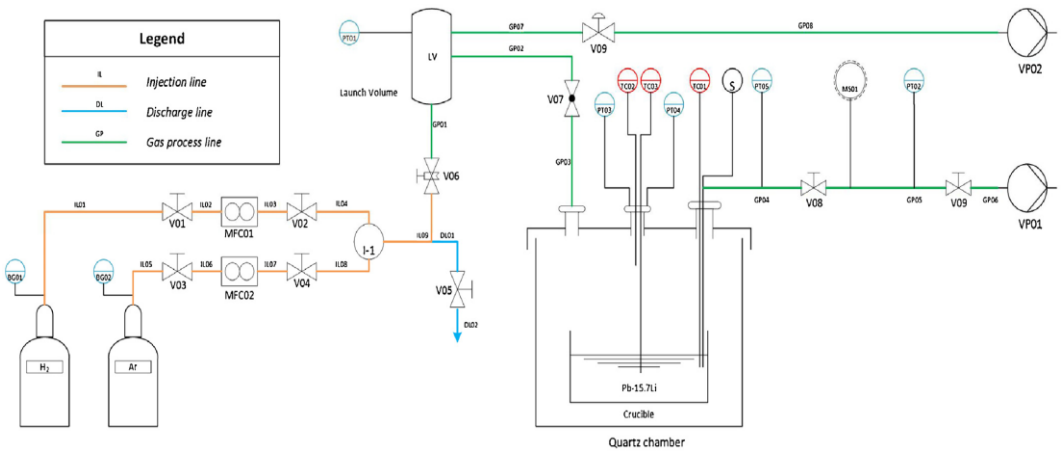

Figure 15 - Hyper-Quarch layout [31].

The main chamber is made in quartz glass. This material has been chosen because of very low permeability to hydrogen [32]. In this way is possible to reduce to the minimum the leakages to the environment, a needed

condition for the working principle of the device. The lithium lead is placed in the tungsten melting pot inside the quartz chamber, where it is kept in liquid phase with external infrared heater that keeps high temperature in all the chamber (max. 550°C). The upper part of the chamber is closed with an AISI 316 steel flange that has three cylindrical sleeves. This choice has been made because of connection issues between the quartz sleeves of the previous upper flange and the rest of the system [31]. The largest of the three hosts the permeation sensors, one at the time for the different tests. The sensor internal is connected to a pressure transducer, a thermocouple and a mass spectrometer to be able to read the concentration of hydrogen that is permeated into the probe. Before each test, the vacuum is made inside the sensor to avoid oxidation that could invalidate the results [31].

In a second sleeve two pressure transducers are connected, to be able to read the pressure inside the chamber, and two thermocouples, one in gas phase and the other in lithium lead. The remaining port is connected to the launch volume, where the gas mixture Ar/H_2 is prepared for the test, at 1.5 bar and 450 °C. The launch volume is connected to cylinder of the two gases and two mass flow controllers allow to choose the concentration of H_2 and Ar for the test. The concentration obtained is read by a thermal conductivity analyser just before the launch volume [31].

To avoid contamination also in the gas mixture and in the chamber, a secondo pumping system is connected to all the circuit to obtain the vacuum everywhere before preparation of the test. Vacuum is obtained thanks to a diaphragm and turbomolecular pump, with an expected ultimate vacuum pressure of 10 mPa [31].

The experimental procedure is quite simple: the gas mixture is fluxed in the quartz chamber and the saturation of the lithium lead occurs. After that, the sensor immersed in the liquid is filled with hydrogen thanks to permeation phenomenon and reach the same equilibrium partial pressure of hydrogen in lithium lead. For gas phase experiments the sensor is placed in contact with gas and follow the same working principle [31].

The experimental results are shown in Table 5.

Table 5 - Test results on Hyper-Quarch device [31].

Test #	Sens. type	Phase	p_{tot} [mbar]	H_2 conc. [%]	T [°C]	p_{eq} [Pa]	Δt [h]
1	Hel.	Gas	870	3.5	380	2967	8.3
2	Hel.	Liquid	870	4	400	3455	12.9
3	Hel.	Liquid	1000	1.4	400	1115	4.3
4	Hel.	Liquid	870	1.2	400	1216	11.4
5	Hel.	Liquid	870	8.5	400	7423	28.3
6	Cyl.	Gas	870	3	380	2342	11.3

The response time Δt is the time needed to reach 90 % of the equilibrium pressure. Unfortunately, during the maintenance of the device the quartz chamber has been broken and not all the tests have been carried out and the cylindrical sensor has been used only for one test in gas phase. From the results obtained can be seen a slower response time for the tests in liquid phase, especially for higher partial pressure of the hydrogen. However, the comparison between the two types of test, gas and liquid phase, cannot lead to definitive conclusions because of the lack of more experiments. In the next section, the permeation sensors are described more in detail.

3.2 Permeation sensors

The sensor working principle is based on the permeation of hydrogen through a metallic membrane and the filling of the internal volume of the probes. It can work in two ways: dynamic and equilibrium mode. In dynamic mode the vacuum is continuously kept inside the sensor and the concentration of hydrogen is measured thanks to the permeation flux evaluation. In the second mode, the hydrogen permeates through the membrane until the equilibrium between the partial pressures on both sides is reached. Knowing the pressure of hydrogen is needed to compute the concentration inside the liquid metal through the Sieverts' law

$$C_{H,PbLi} = K_{S,PbLi} \cdot \sqrt{p_{H,eq.}} \tag{3.1}$$

where $C_{H,PbLi}$ [mol/m^3] is the concentration of hydrogen in lithium-lead, K_S [mol/m^3/Pa$^{0.5}$] is the Sieverts' constant or solubility of hydrogen in lithium-lead and $p_{H,eq.}$ [Pa] is the equilibrium partial pressure of hydrogen in lithium-lead. At the equilibrium, the pressure in the sensor is equal to the

one inside the PbLi, so that knowing the solubility it is possible to calculate the concentration [33]. The characteristics of an optimal sensor design are [34]:

- *High permeability*: this characteristic allows faster pressurization of the sensor that means faster response time.
- *High diffusivity*: a material with high diffusivity and low solubility is preferable because of the correlation

$$\phi = K_S \cdot D \tag{3.2}$$

  where ϕ [mol/m/s/Pa$^{0.5}$] is the permeability and D [m^2/s] is the diffusivity. A low solubility means lower quantities of hydrogen dissolved in the membrane of the sensor and high diffusivity means a faster response.

- *Chemical compatibility*: the capsule must be immersed in lithium-lead, so a suitable material must be chosen, especially for corrosion issues.
- *High S/V ratio*: this geometrical constraint is needed to maximize as much as possible the surface available for permeation and to minimize the internal volume of the sensor, in order to have a faster response.
- *Small internal volume*: the dead volume should be small to reduce the time needed to reach the balance because the pressurization occurs faster.

After the identification of these characteristics for the sensor, a first qualification was made in a previous experimental campaign with respect to Hyper-Quarch. This type of sensor can work in two different modes: equilibrium and dynamic. The first relies on reaching the equilibrium between the partial pressure of hydrogen in both sides of the sensor, starting from a vacuum condition in the internal volume of the probe. In the second mode, the vacuum is continuously kept inside the sensor and the concentration of hydrogen is measured through the rate of permeation through the membrane [33]. In Hyper-Quarch experimental campaign, the sensors have been tested in equilibrium mode [31].

The chosen materials for the previous experimental campaign were Fe and Nb with a cylindrical form of the sensor [33]. Unfortunately, the results

were not optimal for Nb sensor in equilibrium mode both for gas phase and liquid phase tests. A much lower value of the equilibrium pressure has been measured respect to the one imposed in gas and liquid and after each test the permeating flux was reducing [33]. This could be explained by the formation of oxide layer on the surface of the sensor and with the high solubility value of Nb (Table 6) [33].

Table 6 - Solubility, permeability and diffusivity of iron and niobium. As can be seen, solubility and permeability of niobium have opposite behaviour as function of temperature respect to iron.

Parameter	**Fe**	**Nb**
Solubility K_S [$\mathrm{mol/m^3/Pa^{0.5}}$]	$0.8 \cdot e^{(-\frac{3700}{T})}$	$0.126 \cdot e^{(\frac{4240}{T})}$ [35]
Permeability ϕ [$\mathrm{mol/m/s/Pa^{0.5}}$]	$4.1e-8 \cdot e^{(-\frac{4200}{T})}$ [35]	$6.3e-9 \cdot e^{(\frac{3010}{T})}$ [35]
Diffusivity D [$\mathrm{m^2/s}$]	$5.12e-8 \cdot e^{(-\frac{500}{T})}$ [36]	$5e-8 \cdot e^{(-\frac{1230}{T})}$ [35]

where T [K] is the temperature and the solubility has been computed as $K_S = \phi/D$.

Even for the iron sensor, the results were not so optimal, with several hours required to reach the equilibrium [33]. However, iron gave a better response working in dynamic mode, because it was able to follow quite rapidly changes in hydrogen concentration [33]. This material was not been discarded as an option and the new campaign on Hyper-Quarch was done with two types of sensor: a cylindrical one, with a filler inside to reduce dead volume, and a helical one to increase the S/V ratio. The first sensor is 40 mm height and a 20 mm diameter and the helical is 30 mm height with the same diameter of the cylinder [31]. The behaviour of the helical and cylindrical sensors in gas phase is shown in Figure 16.

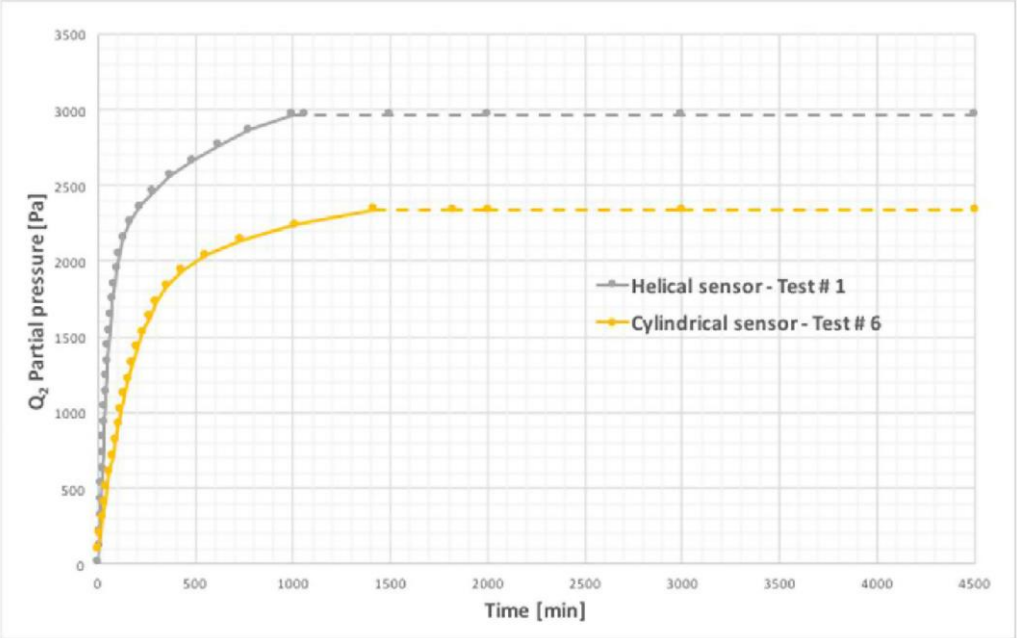

Figure 16 - Sensor pressure as a function of time in the two tests done in gas phase during Hyper-Quarch campaign [31].

As it can be seen, the response time is of the order of several hours, but faster pressurization can be seen for the helical sensor, the one with the highest S/V ratio.

The same type of helical sensor has been adopted in TRIEX-II facility built in C. R. ENEA Brasimone between 2018 and 2019 (section 4.3). The geometry of the sensor is specified in Table 7.

Table 7 - Helical sensor geometrical parameters [37].

Parameter	**Value**	**U.o.M.**
Height	40	[mm]
Major diameter [mm]	40	[mm]
Minor diameter [mm]	2	[mm]
Wall thickness [mm]	0.2	[mm]
Total length [mm]	1000	[mm]
S/V ratio [1/m]	3125	[1/m]
Number of coils	7	

In TRIEX-II three permeation sensors have been positioned in the lithium-lead loop. A picture of these sensors can be seen in Figure 17.

Figure 17 - Helical iron sensors for TRIEX-II. They are placed in a concentric way in the same measurement place.

3.3 Mathematical description of gas phase model

A mathematical model for the sensor functioning in gas phase has been developed. The permeation of hydrogen through a membrane is induced by the gradient of pressure between the two sides. In the case of a metallic membrane, the diatomic hydrogen in gas phase dissociates on the metal surface and becomes monoatomic. At the same time, atomic hydrogen can recombine to its molecular form and detach from the membrane, returning to gas phase. In parallel to these phenomena, diffusion in the gas and through the membrane occurs following the diffusion equation [38]. Finally, two regimes can be distinguished: diffusion-limited and surface-limited. To recognize in which condition is occurring the gas driven permeation, the permeation parameter W_H has been introduced [39]

$$W_H = \frac{K_d \, x \, \sqrt{p}}{D \, K_S} \tag{3.3}$$

where K_d [mol/s/m^2/Pa] is the dissociation constant for the material of the membrane, x [m] is the thickness of the membrane, p [Pa] is the value of high-pressure side and D [m^2/s] is the diffusivity in the membrane. If $W_H \ll 1$ the regime is surface-limited, the surface phenomena are dominating the

process and are the slowest. Instead, if $W_H \gg 1$ the regime is diffusion-limited so that the diffusion process is the slowest and dominating one [39]. With $W_H \sim 1$ a transition regime is occurring, with both surface and diffusion processes that are occurring with the same velocity and must be considered together. In general, three main fluxes can be defined [39]

$$J_d = K_d\, p \tag{3.4}$$

$$J_r = K_r\, C^2 \tag{3.5}$$

$$J = -D\,\frac{\partial C}{\partial x} \tag{3.6}$$

where J_d [mol/m^2/s] is the dissociation flux, p [Pa] is the partial pressure in the bulk of the gas side of the permeating species, J_r [mol/m^2/s] is the recombination flux, K_r [m^4/mol/s] is the recombination constant and J [mol/m^2/s] is the diffusive flux according to Fick's law. In the case of gas phase experiments, the dissociation and recombination fluxes must be considered on both sides of the membrane (Figure 18).

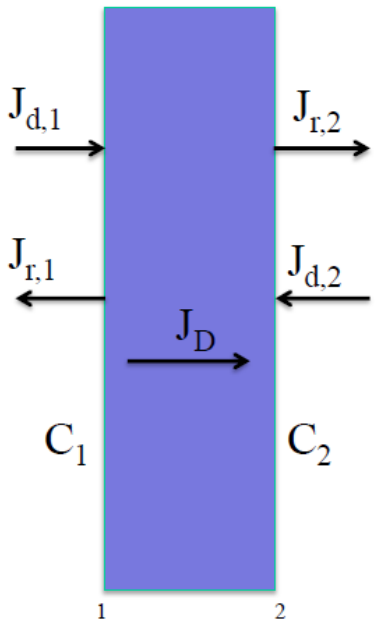

Figure 18 - Representation of the fluxes involved in a gas driven permeation in equilibrium mode. In dynamic mode there would not be the dissociation flux on low-pressure side [40].

Eqs. (3.4-3.5) refer to molecular hydrogen, so that at the boundary with the metallic membrane the relation (3.7) must be kept into account

$$J_H = 2 \cdot J_{H_2} \tag{3.7}$$

In this way, the total molar flux for monoatomic hydrogen is doubled. Also, the sign of the fluxes must be kept into account. In fact, the dissociation flux on the low-pressure side (subscript 2) has a negative contribution to the pressurization of the sensor while the recombination one has a positive contribution. From the high-pressure side (subscript 1) the logic is inverse, always considering the pressurization of the sensor volume as the final goal. The total fluxes imposed on the two boundaries of the membrane are explicated in Eqs. (3.8-3.9).

$$J_{H,1} = 2 \cdot (K_d p - K_r C_H^2) \tag{3.8}$$

$$J_{H,2} = 2 \cdot (K_r C_H^2 - K_d p) \tag{3.9}$$

In steady-state condition is possible to write a relation between the recombination and the dissociation constants. At the equilibrium, the pressure is the same everywhere and there is no more concentration gradient so that the surface phenomena compensate each other.

$$K_r \, C^2 = K_d \, p \tag{3.10}$$

Using the Sieverts' law in eq. (3.1) is possible to write

$$K_r K_s^2 = K_d \tag{3.11}$$

The relation in Eq. (3.11) allow the computation of one of the two constants thanks to the other. Finding in literature the solubility of the materials is easier than find both the constants of recombination and dissociation because are quite difficult to measure experimentally or to compute [41].

At the boundary, the continuity of the pressure must be kept so that.

$$p_{H_2,1} = p_{H,Fe,1} \tag{3.12}$$

At the interface between the gas and the metal, the pressure can be considered the same. Writing the pressure with the gas law for $p_{H_2,1}$ and using Sieverts' law for $p_{H,Fe,1}$ the eq. (3.13) is obtained

$$C_{H_2,1} R \, T = C_{H,Fe,1}^2 / K_{S,Fe}^2 \tag{3.13}$$

where R [J/mol/K] is the universal gas constant, T [K] is the absolute temperature of the gas and $K_{S,Fe}$ [mol/m^3/Pa$^{0.5}$] is the solubility of hydrogen in iron. In this way, a correlation between the concentrations at the interface is obtained.

3.4 Results and discussion

The mathematical model described has been implemented using COMSOL Multiphysics software. The geometry used for the simulation is represented in Figure 19.

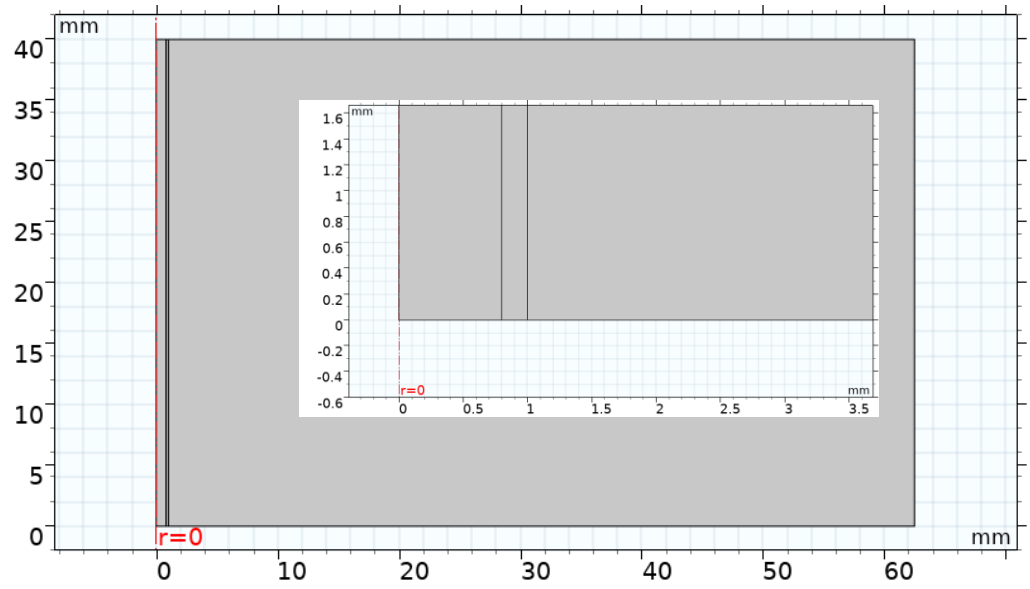

Figure 19 - COMSOL 2D geometry for the iron sensor simulation with a zoom of the sensor boundaries.

The geometry chosen is 2D-axisymmetric respect to r=0 axis. The right side represents the chamber full of gas while the left side is the sensor internal together with the membrane thickness. The simulations have been adapted to the case of two sensors installed in TRIEX-II facility, the HLM734 and HLM735, respectively placed at the outlet of saturator and extractor. The transport and input data set in the simulations are shown respectively in Table 8 and Table 9.

Table 8 – Main transport parameters.

Parameter	Value or correlation	U.o.M.
Solubility of hydrogen in iron, $K_{S,Fe}$	$0.8 \cdot e^{(-\frac{3700}{T})}$	$[mol/m^3/Pa^{0.5}]$
Permeability of hydrogen in iron, $\phi_{H,Fe}$	$4.1e-8 \cdot e^{(-\frac{4200}{T})}$ [35]	$[mol/m/s/Pa^{0.5}]$
Diffusivity of hydrogen in iron, $D_{H,Fe}$	$5.12e-8 \cdot e^{(-\frac{500}{T})}$ [36]	$[m^2/s]$
Recombination constant, $K_{r,Fe}$	$3e-27 \cdot N_A$ [41]	$[m^4/mol/s]$
Dissociation constant, $K_{d,Fe}$	$1.95e-8$	$[mol/s/m^2/Pa]$

Table 9 - Input parameters for HLM734 and HLM735 simulations.

Parameter	Value	U.o.M.
Temperature, T	673.15	[K]
Sensor internal diameter	1.6	[mm]
Sensor wall thickness	0.2	[mm]
Hydrogen initial concentration in iron membrane and HLM734 sensor volume	0	[mol/m^3]
Hydrogen initial concentration in iron membrane and HLM735 sensor volume	0	[mol/m^3]
Permeation parameter for HLM734, W_H	0.84	
Permeation parameter for HLM735, W_H	0.93	

The results are shown in Figure 20 and Figure 21.

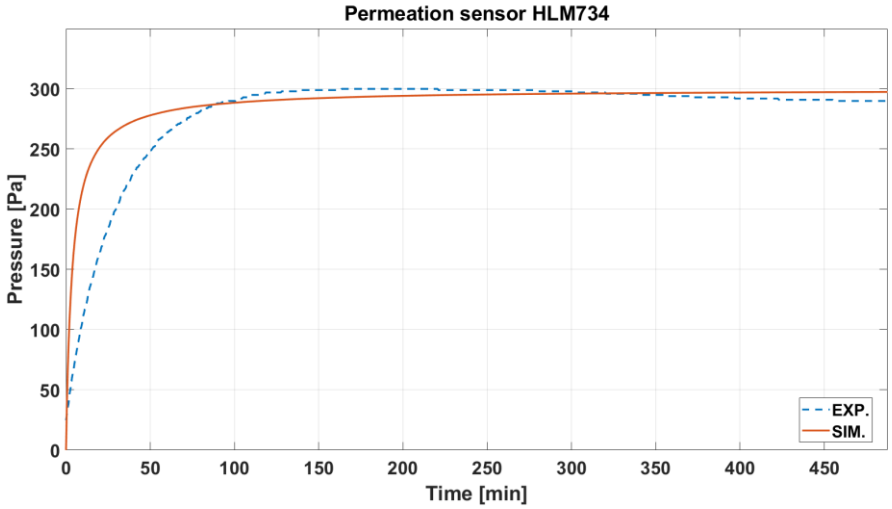

Figure 20 - Simulation result for HLM734 sensor.

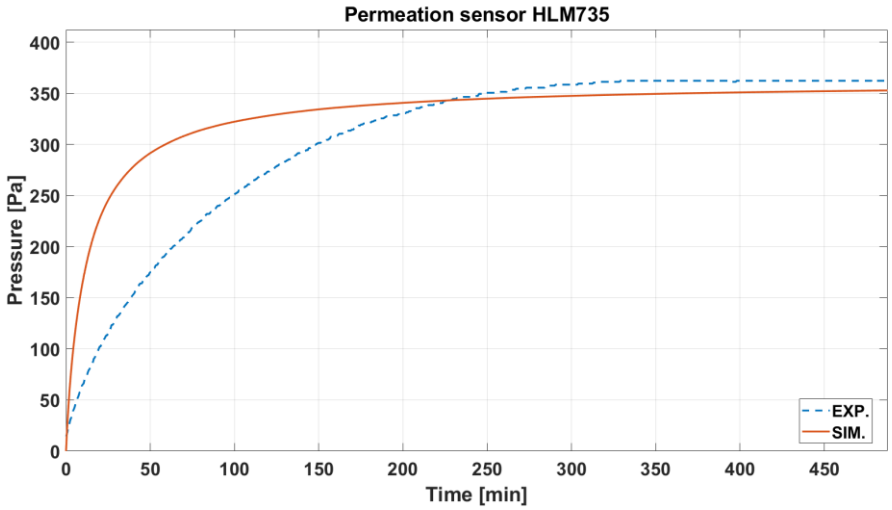

Figure 21 - Simulation result for HLM735 sensor in gas phase.

As it can be seen, the fitting of the experimental curve and the simulation are better for HLM734 sensor. For the HLM735 sensor, there is a good response regarding the final equilibrium pressure but the time to reach it is a bit different. However, the response time is quite different between the experimental and simulation curves. So, a sensitivity analysis has been done on the permeation parameter changing the value of the Sieverts' constant and keeping constants the other values. This parameter is fundamental in the calculation because is used to correlate the concentration with the pressure and in calculation often is elevated to the second power, so a slight change on the solubility could lead to significant variations in the results. After the calculation of the optimal values for the permeation parameter, three types of error have been calculated: the integral error, the relative errors on the response time of the sensor and on the final pressure reached. The error on the response time has been calculated considering the time needed to reach 90 % of the equilibrium value [37].

$$err_{int} = \left| 1 - \frac{\int_{t_0}^{t_{end}} p_{H_2,sim}(t)dt}{\int_{t_0}^{t_{end}} p_{H_2,exp}(t)dt} \right| \tag{3.14}$$

$$err_t = \left| 1 - \frac{t^*_{sim}}{t^*_{exp}} \right| \tag{3.15}$$

$$err_p = \left| 1 - \frac{p_{end,sim}}{p_{end,exp}} \right| \tag{3.16}$$

The results are shown in Table 10 and the new behaviour of the simulations respect to experimental values is shown in Figure 22.

Table 10 - Error calculation for the gas phase model [37].

Parameter	**HLM734**	**HLM735**
Response time (experimental), t^*_{exp} [min]	64	185
Theoretical permeation parameter, W_H [-]	0.843	0.927
Best fit permeation parameter, W^*_H [-]	2.667	4.145
Integral error, err_{int} [%]	0.41	4.07
Response time error, err_t [%]	4.69	3.24
Accuracy error, err_p [%]	1.86	6.09

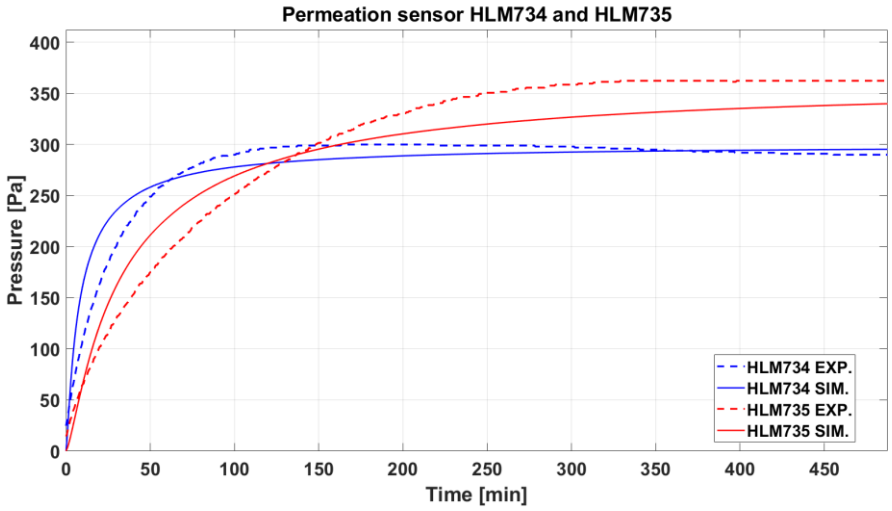

Figure 22 - Permeation sensors trend with the optimal value of the permeation parameter.

With the optimal values of the permeation parameter, the errors are very low, below 10%. As can be seen, the sensors work in a mixed regime because the permeation parameter is around the unity. In this case, consider pure diffusion lead to mistakes because the surface phenomena slow down the permeation process. The main issue is to implement surface phenomena in a mathematical model. The parameters that govern the interaction with the metallic membrane, K_d and K_r are difficult to calculate [41]. Moreover, the link between the two is the Sieverts' constant, that is also affected by multiple uncertainties [42]. In the liquid phase functioning the problem of the solubility is doubled because also one of the lithium-lead must be known. This is the reason why a new device, Hyper-Quarch-II, will be built to have new measurements of the Sieverts' constant of hydrogen in lithium-lead.

3.5 Solubility measurement: Hyper-Quarch-II

The previous experimental campaign on Hyper-Quarch was interrupted due to a rupture of the quartz chamber of one of the sleeves. Only six tests were carried out and the new helical sensor gave better response respect to the cylindrical one. Due to the low number of tests a new device Hyper-Quarch-II will be developed with a very similar and new instrumentations. The upper flange has been re-designed and it will be always in quartz glass. A 3D view of the flange can be seen in Figure 23.

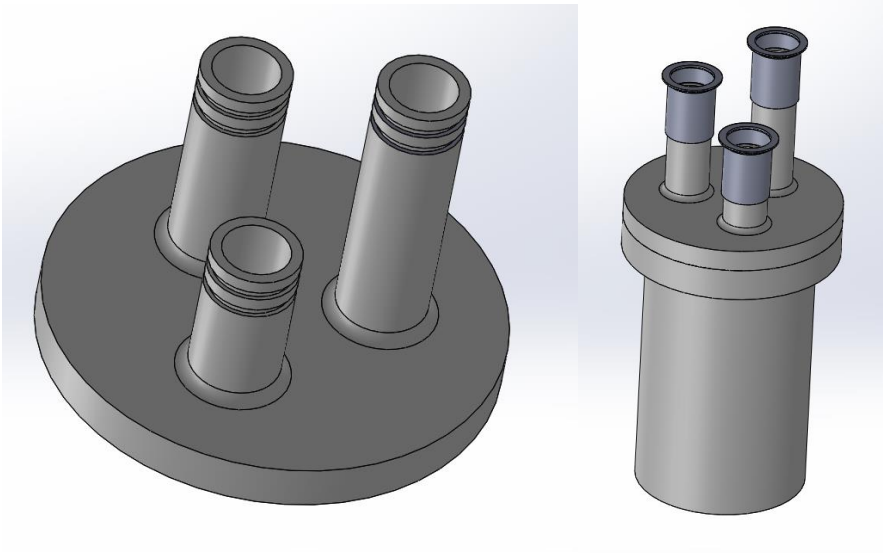

Figure 23 - 3D view of the upper flange of the quartz chamber (left) and total assemble with steel connections (right).

The sleeves on the upper flange have been designed with different height because of the space needed to place the connections and the steel ties. The three couplings will have the same functions. One will be used for the permeation sensor, one for the measurement of pressure and temperature in the sample of lithium-lead and the chamber and the last one for the injection of the gas mixture. A completely new pipeline will be installed together with a new vacuum system and mass flow controllers with their relative Data Collection Unit. A new test matrix will be developed. The experiments will involve the helical sensors, changing the number of coils to investigate if this influences the response time, and the cylindrical sensor with a coated filling to reduce the dead volume.

Beyond the more detailed qualification of the permeation sensors, the device will be used for a new measure of hydrogen solubility in lithium-lead, so the test will be performed at different temperatures. The measure of the Sieverts' constant can be done following two technique: absorption and desorption [32]. In the first case, a high vacuum is done in the chamber. After that, a known amount of hydrogen is inserted and the steady-state condition must be waited. The difference in pressure in the gas gives the amount of hydrogen solubilized in the lithium-lead so that the solubility can be computed thanks to Eq. (3.17)

$$K_{S,PbLi} = \frac{2\,(p_0 - p_{end})\,V_{gas}}{R\,T\,V_{PbLi}\,\sqrt{p_{end}}} \tag{3.17}$$

where p_0 [Pa] is the initial pressure of hydrogen, p_{end} [Pa] is the pressure at the steady-state, V_{gas} [m^3] is the volume of gas and V_{PbLi} [m^3] is the volume of lithium-lead sample used in the experiment. The doubling factor is needed to keep into account the dissociation of hydrogen molecules dissolved in lithium-lead [32]. The desorption technique is based on the release of hydrogen in a well-known volume from a sample that was previously saturated with a known concentration of hydrogen. Thanks to the pressure increase in the gas, it is possible to compute the solubility of the lithium-lead sample.

Different experimental activities have been carried out for the measuring of the Sieverts' constant [43] [44] [45] [46]. The main recognized factors that influence the results are:

- Alloy purity;
- Melting procedure: possible formation of impurities;
- Alloy state: homogeneity, convection, bubbling, thermal gradients;
- Loading of the alloy into the melting pot;
- Sample contamination: not high vacuum condition or sealing of the volume can lead to contamination;
- Hydrogen purity;
- Method of measurements and registration;

These multiple factors must be kept into account for the design of an experimental device and during the experimental campaign.

4 Characterisation of Tritium Extraction System

Tritium is one of the two isotopes that takes part to fusion reaction. Because of its short half-life it must be produced on situ and this is one the functions of the blanket. The Tritium Breeding Ratio (TBR) definition has been introduced for the breeding zone. Parasitic captures and losses must be considered inside the blanket, so that not all the neutrons coming from the plasma will interact with Li to produce T. Moreover, the TBR must be higher than the unity because the TER system will not extract all the tritium produced, but a minimum quantity must be recovered to keep a sufficient fuel source for the fusion reaction. Consequently, a suitable highly efficient extraction system has to be developed for the PbLi cycle in order to recover the tritium produced needed for the fuel cycle and also for having the minimum inventory, because of safety issues. Different technological solutions could be possible, such as getters, tritium permeators and gas-liquid contactors (GLCs) [47]. On this last topic, more experimental efforts have been done [48] because of the simpler technological requirement of GLCs respect to other technologies. Even if bubble and spray columns had very low efficiency, the packed column technology has given better results [49] [50]. For this reason, this variant of GLCs has been studied as a possible candidate for fusion applications with an experimental facility called TRIEX, developed at C. R. ENEA Brasimone in 2006, and its successor TRIEX-II, built in the same place between 2018 and 2019. In the further sections the basics of the GLCs with the layout of the two facilities will be shown.

4.1 Gas Liquid Contactor

In a gas liquid contactor, a liquid and a gas mixture are put into contact. GLC can work in two ways: as an absorption column and a desorption column. In the first case, the soluble substance in the gas mixture is dissolved in the liquid and in the second case a stripping gas is used to desorb the substance from the liquid [51]. This type of equipment is especially used in chemical industry but has become promising for liquid metal blankets for tritium extraction, especially for the ITER project.

Between GLCs, there are different technologies that work with different principles.

- *Falling-film or wetted-wall columns*: in this configuration the liquid flows from the top to the bottom along the wall of a vertical tube forming a thin film and the gas is in counter-current in the centre, as can be seen in **Errore. L'origine riferimento non è stata trovata.**. They are used for mass and heat transfer mostly in laboratory applications because of easiness of modelling and low gas-liquid surface interface [52].

- *Spray columns or towers*: gas liquid contactor that transfer mass and heat between a continuous gas phase and dispersed liquid phase. Usually the gas is streamed from the bottom while the liquid is sprayed from above at different height levels. The droplets must not be too small in order to avoid that gas take away the liquid in the upward flow, but smaller they are and higher is the efficiency because of higher contact surface between the phases. In some configurations the gas is streamed to produce some cyclonic motion because higher velocities mean more effective particles and droplets separation and higher collection efficiency. This type of technology is especially used in pollutants removal from gas phase. They are also used for gas absorption but with less efficiency than plate or packed columns [53].

- *Plate or tray columns*: used typically in distillation, in this type of GLC liquid and gas phases come in contact at different stages. Each of these stages is delimited by a plate, except the one at the top and at the bottom. In this way the liquid is forced to flow horizontally at each stage and the vapor goes upward through holes in the trays. The purpose of this is to increase the time and the surface area in which the two phases stay in contact.

- *Bubble columns*: in a cylindrical vertical vessel full of liquid the gas is streamed from the bottom and through a sparger create a turbulent flow in the column. It can flow in parallel or counter-current. Bubble columns are characterized by a high amount of liquid and small fraction of gas.

The contact surface is determined by the number and size of bubble of the gas [54]. In Figure 24 is possible to see the design of a bubble column.

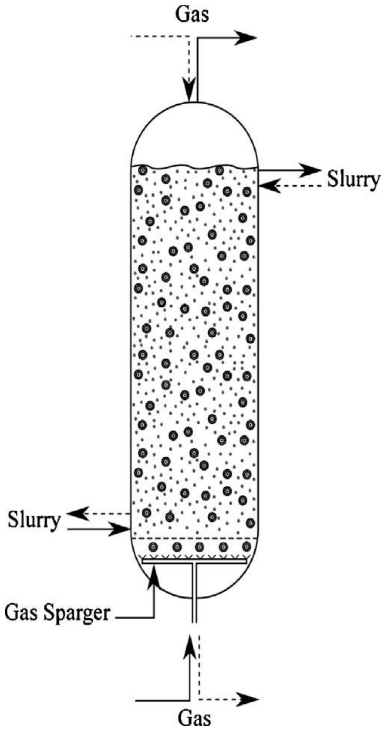

Figure 24 - Bubble column design. [55]

- *Packed columns*: in packed towers, liquid and gas are in continuous contact, differently from the tray columns. They provide a large amount of surface area per unit volume in order to maximize and facilitate the mass transfer between the two phases. There are two main types of packed tower: random packing and structured packing, that are shown in Figure 25.

Figure 25 - Random packing pall rings [56] and structured packing metal sheets. [57]

The first one can be in metallic or non-metallic materials and are used in distillation processes. They have not a specific geometry or scheme for the filling material and they were the first to be developed. The structured packing relies on a more precise geometry of the materials like corrugated and perforated sheets in metal or plastic. This configuration allows a very low pressure drop and a good spreading of the liquid flow, with different benefits in low pressure and low flow rates condition [58]. These are the reasons because structured filler has been chosen for TRIEX and TRIEX II facility. Moreover, good results were obtained testing packed column efficiency with lithium-lead in other experimental campaigns [49] [50], choosing to deep the characterisation of this technology. The design of a packed column is shown in Figure 26.

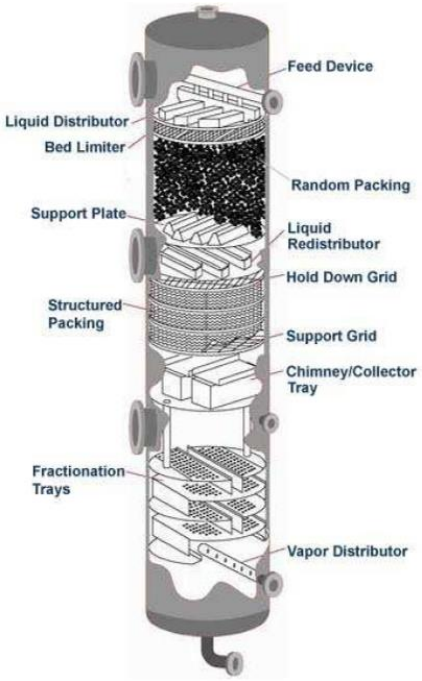

Figure 26 - Packed column design. [59]

4.1.1 Packed column design

There are different methods for the estimation of the height of the active part of a packed tower. They are all based on mass transfer between the materials interface and their balances. This procedure leads to an integral expression to calculate the number of theoretical stages and transfer

units. The mass-transfer-rate expression is the more general mode to compute the height of a transfer units, but it is the most complex because has a derivative form over the height of the column [60]

$$N_A' \, A \, dz \, a = k_G \, a \, (P_{AG} - P_{Ai}) \, A \, dz \tag{4.1}$$

$$N_A' \, A \, dz \, a = k_L \, a \, (C_{Ai} - C_{AL}) \, A \, dz \tag{4.2}$$

where N_A' [mol/m^2/s] is are the mole of solute absorbed per unit time and area, A [m^2] is the cross section of the column, z [m] is the height of the column, a [m^2/m^3] is the packing factor, k_G [mol/m^2/s/Pa] and k_L [m/s] are the mass transfer coefficient of the gas and liquid respectively, P_{AG}[Pa] and P_{Ai} [Pa] are the partial pressure of the solute A in the bulk and at the interface in gas, C_{AL}[mol/m^3] and C_{Ai} [mol/m^3] are the concentration of the solute A in the bulk and at the interface in liquid.

In this case, the mass transfer coefficient of the two substances should be known and also the value of the concentrations of the solute at the bulk and at the interface, that are quite different as can be seen in Figure 27.

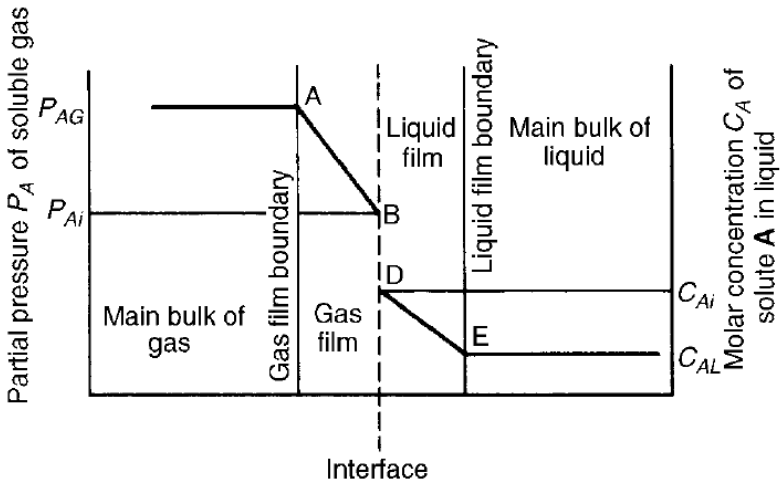

Figure 27 - Gas-Liquid interface conditions for a certain solute A. [60]

Frequently, an easier way to compute the height of the transfer units is to start writing the balance between the two phases, obtaining the operating curve. The operating curve is the line that correlates the molar fraction of solute in the gas with the one in the liquid in operating conditions. It is possible to write it referring to Figure 28.

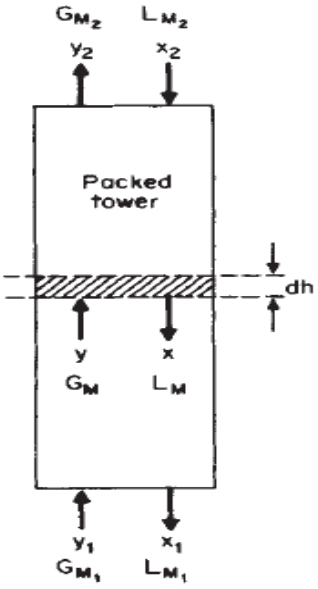

Figure 28 - Gas-liquid balance in a packed column. [51]

From the local balance written in differential way, it is possible to write the operating curve at a general height of the column

$$G_M(y - y_2) = L_M(x - x_2) \tag{4.3}$$

where G_M [mol/s] is the molar gas flow rate, y is the molar fraction of the solute in gas phase at a certain height h, y_2 is the outlet molar concentration of the solute in gas phase, L_M [mol/s] is the molar liquid flow rate, x is the molar fraction of the solute in the liquid phase at a certain height h and x_2 is the inlet molar fraction of the solute in the liquid phase [51].

Eq. (4.3) can be used only with dilute solutions so that flow rates are nearly constant. The operating curve is approximated as a straight line and is different from the equilibrium curve, as it can be seen in Figure 29.

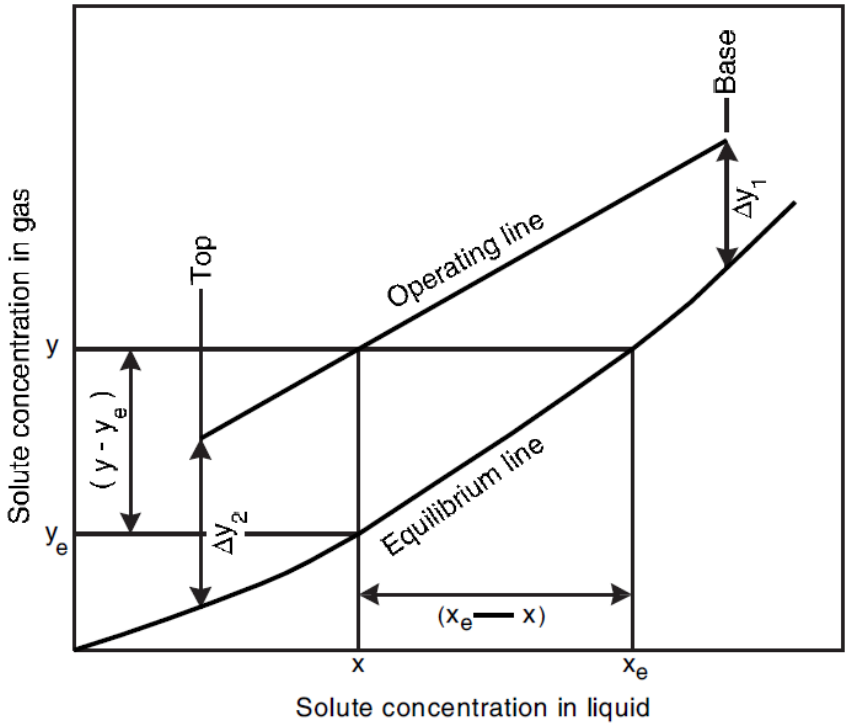

Figure 29 - Equilibrium and operating line. [61]

The slope of the line that connects the two curves is determined by the ratio of the local mass transfer coefficients of the solute in liquid and gas [51]. The problem is that knowing the mass transfer coefficients at each height of the column is very difficult, so it is not easy to compute the concentration on the equilibrium curve. It is more convenient to have an integral form in order to calculate the height. Eqs. (4.4-4.5) are derived from general Eqs. (4.1-4.2) [61]

$$Z = \frac{G_M}{K_G\, a\, P} \int_{y_2}^{y_1} \frac{dy}{y - y_e} \tag{4.4}$$

$$Z = \frac{L_M}{K_L\, a\, C_t} \int_{x_2}^{x_1} \frac{dx}{x_e - x} \tag{4.5}$$

where K_g [mol · m/s/Pa] and K_l [m^4/s] are the overall mass transfer coefficients of gas and liquid, P [Pa] is the total pressure of the gas, y_e and x_e are the molar fraction of the solute in gas and liquid respectively on the equilibrium curve, C_t [mol/m^3] is the total concentration of the liquid. Another way to write these two equations is in term of "transfer units", easier to handle for design purposes. "Transfer units" are the hypothetical

stages needed to transfer one unit of the solute from the concentrated solution to the stripping one. It is possible to distinguish between the height of the single "transfer unit" and the number of "transfer unit" needed to have a certain efficiency

$$Z = H_{OG}\, N_{OG} \;\; or \; Z = H_{OL}\, N_{OL} \tag{4.6}$$

$$H_{OG} = \frac{G_M}{K_G\, a\, P} \;\; and \;\; N_{OG} = \int_{y_2}^{y_1} \frac{dy}{y - y_e} \tag{4.7}$$

$$H_{OL} = \frac{L_M}{K_L\, a\, C_t} \;\; and \;\; N_{OL} = \int_{x_2}^{x_1} \frac{dx}{x_e - x} \tag{4.8}$$

where H_{OG} and H_{OL} are the heights of overall gas and liquid transfer units respectively [m], N_{OG} and N_{OL} are the numbers of overall gas and liquid transfer units respectively. In general, H_{OG}, H_{OL}, N_{OG}, N_{OL} are called HTU (Height of Transfer Unit) and NTU (Number of Transfer Unit) [61].

If the operating and equilibrium curve can be taken as straight lines and the liquid is almost solute free, N_{OG} can be computed with Eq. (4.9) [51].

$$N_{OG} = \frac{1}{1 - \left(m \frac{G_M}{L_M}\right)} \ln\left[\left(1 - m \frac{G_M}{L_M}\right) \frac{(y_1 - m\, x_2)}{(y_2 - m\, x_2)} + m \frac{G_M}{L_M}\right] \tag{4.9}$$

Where m is the slope of the equilibrium curve. An analogue formula can be written for N_{OL} [51].

$$N_{OL} = \frac{1}{1 - \left(\frac{L_M}{m\, G_M}\right)} \ln\left[\left(1 - \frac{L_M}{m\, G_M}\right) \frac{(x_2 - y_1/m)}{(x_1 - y_1/m)} + m \frac{G_M}{L_M}\right] \tag{4.10}$$

The value HTU has no univocal way to be determined, because it depends not only on physical properties but also on gas and liquid flow rates that depend on the uniformity of the two solvent and their distribution inside the column, which are affected by the geometry of the column itself. Different experimental values and correlations are present in literature, like the one of *Cornell et al.* (1960), *Eckert* (1963) and *Vital et al.* (1984). They are based on empirical correlations in order to calculate the height of transfer units of gas and liquid phases [61].

Another important geometric parameter is the diameter of the column. Usually this is determined from the flooding condition, which is a situation that should not happen inside an absorption column. In flooding condition, the flow of gas is high enough to impede the liquid fall so that it cannot reach anymore the bottom of the column. This situation is recognizable by a sharp rise of the pressure drop and liquid holdup and a sharp decrease of the efficiency. There are different empirical correlations to predict flooding conditions and pressure drops. These are useful to determine the minimum diameter of the column to avoid the flooding gas flow rate G_{FL}. Correlations allow the calculation of G_{FL} and normally the choice of the diameter is done supposing a gas flow rate of a certain fraction of G_{FL}, around 60-80%. A larger diameter allows also better redistribution of liquid and gas flow rates and lower pressure drops. Often a safety factor is also considered so that in operating conditions is very difficult to reach the flooding point. Example of correlations and graphics used to predict flooding point can be found in [61].

4.2 TRIEX facility: layout and criticalities

In order to study the GLC technology to remove tritium from PbLi, TRIEX facility has been built at C. R. ENEA Brasimone in 2006. The layout of the facility is shown in Figure 30, where it is possible to see the control system.

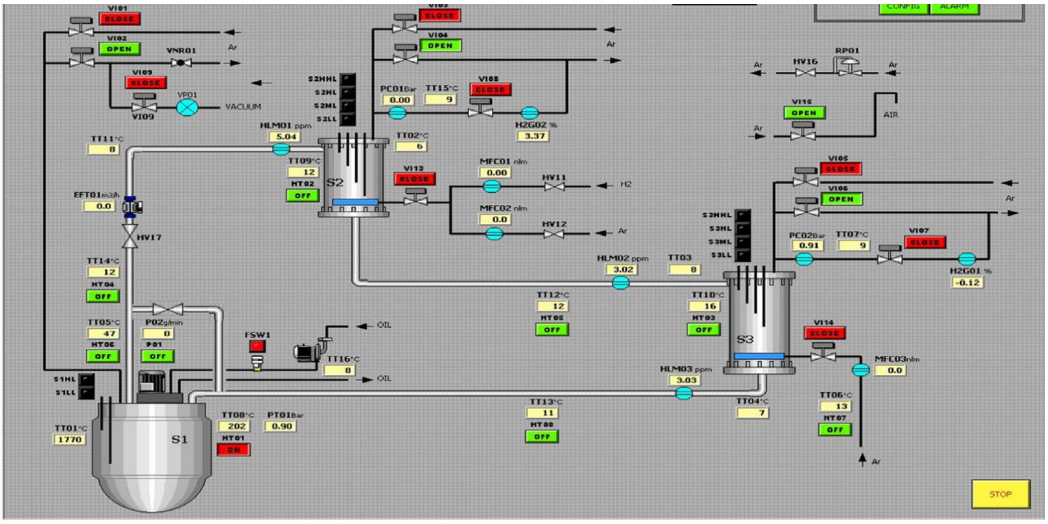

Figure 30 - Control system of TRIEX [47].

The plant is divided in two main loops: lead lithium loop and the gas circuit. The first one is composed by three main components: the storage tank (S1), the saturator (S2) and the extractor (S3). The second loop is used to inject hydrogen in S2 and gas sensors are present.

4.2.1 Liquid metal loop

The lead lithium circuit has been built in ASTM A335 alloy in order to avoid strong corrosion from the liquid alloy circulation. The main components are:

- *Recirculation tank S1*: it is placed at the lowest level for gravity drainage of the alloy and it contains a centrifugal pump P with vertical axis and immersed impeller [47] [48].

- *Hydrogen saturator S2*: it is a tubular tank in which H is injected from the bottom while the liquid falls from the top. H concentration at the outlet is expected to be in thermodynamic equilibrium with H_2 partial pressure in the gas mixture. The gas mixture Ar+H_2 is inserted through a PORAL filter with small channels, to ensure small bubbles and to have a homogeneous gas distribution. A structured packing is placed inside the column to enhance gas-liquid interface. A fluid-dynamic analysis was conducted to choose the optimal values of heights and diameters of the column trough iterative procedures. Temperature of operation was assumed to be 723 K. After all computations and safety factor addition, the final results consist in a height of 35 cm and an internal diameter of 10.2 cm [47] [48].

- *Extractor column S3*: it works in counter-flow and is used for the stripping of the hydrogen from PbLi. The stripping gas is Argon, that is injected from the bottom. A PORAL sintered steel disc is present to uniformly distributes and fragments the gas bubbles.
  Through a fluid dynamic analysis and iterative procedures similar to the one adopted for S2, it has been possible to determine several parameters. Diameter of the column must be large enough to reduce pressure drop

and has to guarantee a continuous and uniform circulation, so a value two times larger of the one determined has been adopted (12.8 cm). This value has been obtained assuming a gas flow rate equal to 60% of flooding flow rate. On the other hand, liquid mass flow rate strongly affects the contact surface for mass transfer processes. A structured filler Baretti B1-350, with packing factor of 350 m^2/m^3 has been mount and minimum and maximum values of flow rate have been fixed according to limits given by the manufacturer. A theoretical column efficiency of 25% has been estimated and height of filler evaluated to be 80 cm, divided in 4 modules of 20 cm in order to study different configurations [47] [48].

4.2.2 Experimental set-up

Inside the liquid metal loop, permeation sensors are immersed in Pbli in order to read the real concentration of hydrogen solubilized. Extraction efficiency is defined as follow:

$$\eta = \frac{C_{in} - C_{out}}{C_{in}} = 1 - \frac{C_{out}}{C_{in}} \tag{4.11}$$

where C_{in} [mol/m^3] is the inlet hydrogen concentration in the lead lithium and C_{out} [mol/m^3] is the outlet hydrogen concentration, evaluated at the inlet and outlet of S3, respectively. An image of these sensors is shown in Figure 31. These three sensors were placed at the inlet and outlet of the extractor and at the inlet of the saturator.

Figure 31 - Cylindrical permeation sensor in pure Fe [48].

The sensor has a cylindrical geometry and it is empty. The material must have a high permeability and low solubility to hydrogen isotopes and iron has been chosen for this purpose. The sensors were manufactured in 99.5% pure α-iron at a design pressure of 7 bar and temperature of 450°C [48]. The working principle is based on reaching the equilibrium between the hydrogen dissolved in PbLi and the hydrogen that permeates inside the hollow chamber of the sensor, which will pressurize. A pressure transducer will give the value of the equilibrium pressure. A vacuum pump is connected to the sensor internal in order to remove the residual hydrogen from the previous test. Since the instruments give a value of pressure, the Sieverts' law is used to compute the concentrations knowing the equilibrium partial pressures, as in Eq. (4.12).

$$C_{H,PbLi} = K_{S,H\_PbLi} \sqrt{p_{H_2,eq}} \tag{4.12}$$

where K_{S,H_PbLi} [mol/m^3/Pa$^{0.5}$] is the solubility of hydrogen in lithium lead and $p_{H2,eq}$ [Pa] is the partial pressure of hydrogen at the equilibrium, read by the pressure transducers installed. The partial pressure is referred to

molecular hydrogen since in gas phase is possible to find H_2, instead in PbLi it dissociates in monoatomic form H. Using this equation is possible to rewrite the efficiency in terms of pressure.

$$\eta = \frac{K_{S,H\_PbLi}\sqrt{p_{H_2,eq_{in}}} - K_{S,H\_PbLi}\sqrt{p_{H_2,eq_{out}}}}{K_{S,H\_PbLi}\sqrt{p_{H_2,eq_{in}}}} = 1 - \frac{\sqrt{p_{H_2,eq_{out}}}}{\sqrt{p_{H_2,eq_{in}}}} \qquad (4.13)$$

The operative conditions of the facility are presented in Table 11 with the efficiencies calculated through the permeation sensors. Three tests were performed [48].

Table 11 - Operative conditions and results of TRIEX experimental campaign.

Test n°	**T [°C]**	**L [kg/s]**	**G [Nl/h]**	**L/G**	**P_H [Pa]**	**η [%]**
1	400	0.38	150	1.15	14300	31
2	400	0.38	100	1.4	8000	10
3	450	0.45	6	34.1	14000	14.7

Different L/G ratio and concentrations of hydrogen have been tested to see how they affects the extraction efficiency.

4.2.3 Design verification

A verification of the column height of the extractor has been carried out in order to compare the result with the real one chosen for the facility. For this purpose, some preliminary data has been taken from [47]. In Table 12 the main input data are reported. Moreover, some calculations have been made to have the needed parameters to be used in the correlations. The extraction efficiency η has been supposed on the basis of real values obtained also in other experimental campaign with packed columns.

Table 12 - TRIEX data and preliminary calculations.

Data	Values	U.o.M.
Efficiency, η	0.30	$[-]$
Inlet molar fraction of H2 in argon, y_1	0	$[\mathrm{mol_{H_2}/mol_{Ar}}]$
Inlet molar fraction of H in PbLi, x_2	$3.86 \cdot 10^{-5}$	$[\mathrm{mol_{H_2}/mol_{Pb-15.7Li}}]$
Flow rate of PbLi, L	0.2	[kg/s]
Flow rate of argon, Q_L	100	[Nl/h]
Temperature, T	723	[K]
Pressure, p	7	[bar]
Section of the column, A_c	0.0129	$[\mathrm{m^2}]$
Specific molar flow rate of PbLi, L_M	0.0884	$[\mathrm{kmol/m^2/s}]$
Specific molar flow rate of argon, G_M	$1.047 \cdot 10^{-4}$	$[\mathrm{kmol/m^2/s}]$
Velocity of PbLi, $v_{Pb-15.7Li}$	0.0016	[m/s]
Velocity of argon, v_{Ar}	$8.994 \cdot 10^{-4}$	[m/s]
Mass-transfer coefficient of Pb-Li, $k_{Pb-15.7Li}$	$1.513 \cdot 10^{-5}$	[m/s]

The mass-transfer coefficient $k_{Pb-15.7Li}$ has been evaluated through the following correlation [62]:

$$k_{Pb-15.7Li} = 2.5 \cdot 10^{-3} \cdot e^{-\frac{30.7}{0.008314 \cdot T}}$$

where T [K] is the absolute temperature. The HTU method has been used, as described in section 4.1.1, with all the needed approximations in order to use the correlations. HTU has been calculated through the mass transfer coefficient and the packing surface [63]

$$HTU = \frac{L_{mol}}{k_{PbLi}\, C_t\, a\, A_c} \tag{4.14}$$

where L_{mol} [mol/s] is the molar flow rate of PbLi and a $[\mathrm{m^2/m^3}]$. is the packing factor of the column.

The angular coefficient of the equilibrium line m can be computed through the Sieverts' law written at the equilibrium at a generic height of the column, as in Eq. (4.15)

$$x_i = \frac{PM_{PbLi}}{\rho_{PbLi}}\, K_{S,H\_PbLi}\, \sqrt{p\, y_i} \tag{4.15}$$

where PM_{PbLi} [kg/mol] is the molecular weight of lithium lead, ρ_{PbLi} [kg/m^3] is the density of lithium lead and p [Pa] is the total pressure from the gas side. The index i refers to a certain point in the column. Then Eq. (4.15) becomes Eq. (4.16) in the form $y_i = f(x_i)$.

$$y_i = \frac{x_i^2}{p}\left(\frac{\rho_{PbLi}}{PM_{PbLi}\,K_{S,H\_PbLi}}\right)^2 \tag{4.16}$$

The slope of this curve is given by the first derivative, equal to searched value m.

$$m = \frac{dy_i}{dx_i} = y_i' = \frac{2\,x_i}{p}\left(\frac{\rho_{PbLi}}{PM_{PbLi}\,K_{S,H\_PbLi}}\right)^2 \tag{4.17}$$

In this way is possible to determine m in each point of the column. For simplification, it has been calculated at outlet condition of the liquid metal, so with x_1 and y_1. Knowing the efficiency, previously supposed, it is possible to write Eq. (4.18) from the definition of efficiency:

$$x_1 = (1-\eta)\,x_2 \tag{4.18}$$

With these conditions and the addition of a safety factor $S = 2$, the active height of the column becomes.

$$Z = S \cdot HTU \cdot NTU = 66.24\ cm \tag{4.19}$$

The value obtained is different from the real one of 80 cm, with a relative error of 17.2%. This result lead to consider a sensitivity analysis on the parameter m, that strongly influences the value of NTU, as seen in Eqs. (4.9-4.10). In Figure 32, it is possible to see the value of NTU as function of m and in Figure 33 can be seen a detail of the plot, where it is possible to observe the difference between the optimal and computed values.

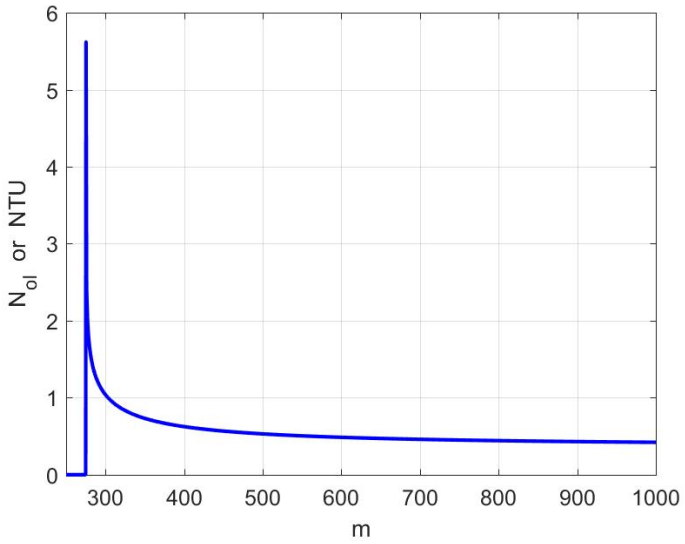

Figure 32 - value of NTU as function of the slope of the equilibrium line. m has been varied with step of 10^-3.

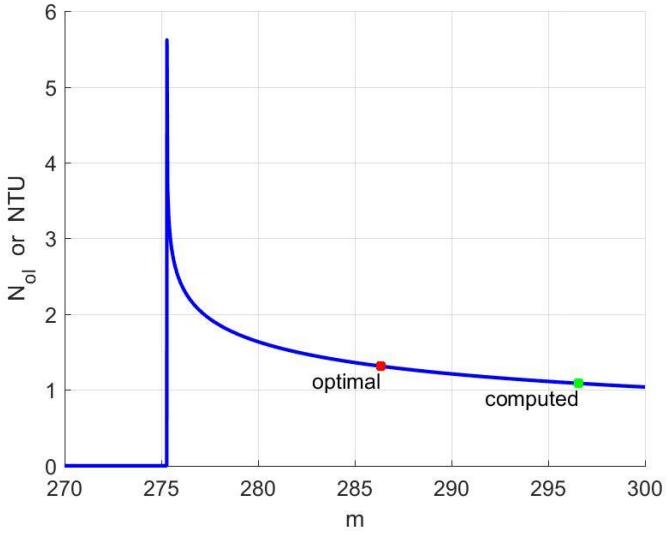

Figure 33 - Comparison between the computed value through the Sieverts' law and the optimal one in order to have the result Z= 80 cm

For high values of m there is not a strong variation of NTU, but for the minimum value, around 275, there is a very sharp increase. This is the proof of the strong influence of m and its calculation, especially near the lower limit that gives real numbers as result.

4.2.4 Criticalities of the facility

From the point of view of the design of the column, the calculation of the optimal active height is a crucial point. The strong approximations applied in computations, particularly in the slope of the equilibrium line m, can lead to significant differences between values computed. This could lead to mistakes in preliminary design that could lead to not optimal experimental results.

From the experimental point of view, the permeation sensors are one of the most crucial points. With only three tests performed, one of them has been oxidized (the one at the inlet of the extractor). Their response time is not always fast and permeability can change drastically if tests are not performed in an optimal way, for example leading to oxidations or ruptures. Another point was the saturation. The saturator S2 was not able to compensate totally the extraction trough S3, so that there was a reduction of the concentration of hydrogen from test 1 to test 2. The saturation seemed to be slower to reach the equilibrium compared to the extraction, that had a faster response of the sensor. Moreover, the lower L/G ratio of the first two tests with a low value of L can cause a reduction of the real contact surface between the two phases, worsening the extraction process and the final efficiency of S3 [48]. Another important aspect is the hydrogen mass balance of all the circuit, that could not be done because the low precision of the instrumentation installed to measure the hydrogen concentration. The sensors were able to respond only for high partial pressures of hydrogen, around 500-5000 appm, but the ones expected in the real TER system in ITER are one order lower, around 10-500 appm [64]. All these issues lead to the design and construction of a more performing facility, TRIEX II, the upgrade of TRIEX.

4.3 TRIEX-II facility: layout and design

Because of the multiple issues found with TRIEX facility, an upgrade of the plant was developed at C. R. ENEA Brasimone during the biennial 2018-2019. As its predecessor, the facility is made of a lead lithium loop and a gas circuit, more elaborated and with a larger volume of the main

components in order to manage higher quantities of PbLi. Moreover, the inert gas chosen for TRIEX-II is He, as in TER design of ITER. In addition, two operational mode have been considered (A and B, respectively): op. mode A is referred to tests performed with hydrogen at the saturator and He at the extractor, op. mode B is refereed to tests performed with He+D2 at the saturator and He+H2 at the extractor, in order to see if there are major differences respect to hydrogen and to be in a condition more similar to reality, where tritium will be the real isotope to extract. A new data acquisition and control system (DACS) was developed for the facility and it is shown in Figure 34.

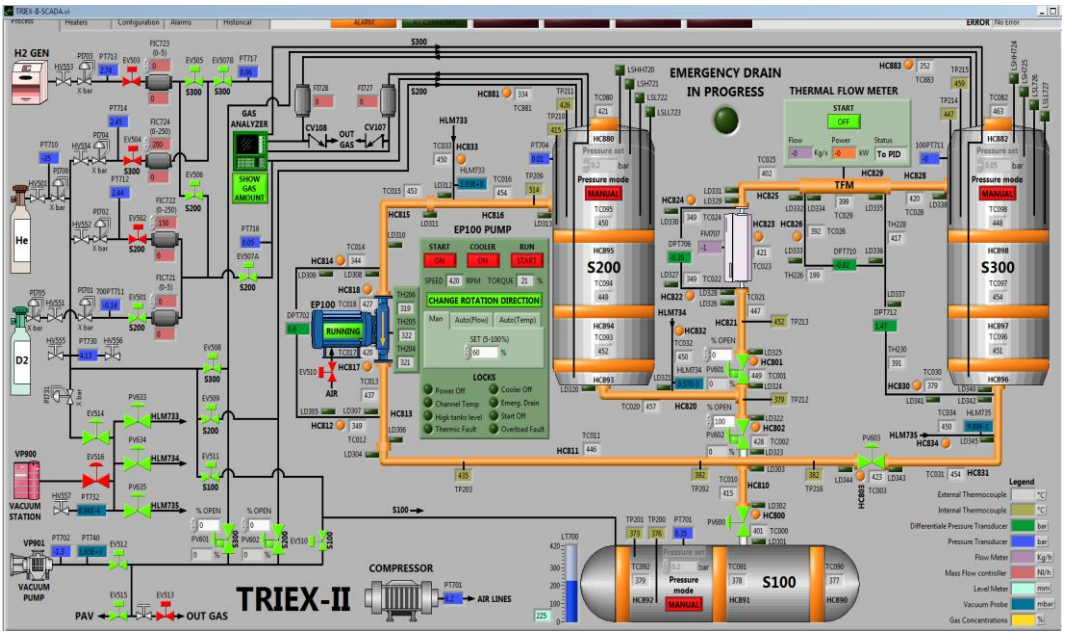

Figure 34 - Synoptic of TRIEX II.

4.3.1 Lead-lithium loop

In Figure 35, it is possible to see the P&ID of the lead-lithium loop of TRIEX II. The main components are the same of TRIEX: the tank S100, the saturator S200 and the extractor S300. One of the main differences is the recirculation pump: in fact, a permanent magnet pump has been adopted in order to avoid leakages of hydrogen and lower load losses, and a by-pass conduit to have a better control on mass flow rate of PbLi [64]. Adjusting

pump rpm modifies the flow rate of liquid metal to the saturator and the entire loop and the by-pass valve change the flow rate to the extractor and the part of the loop that involves it. With two different flow rates to S200 and S300 is possible to balance extraction and saturation phenomena and reach a stable steady-state condition. By-pass branch has also been built to allow an easier and complete drainage of the loop when it is off operation.

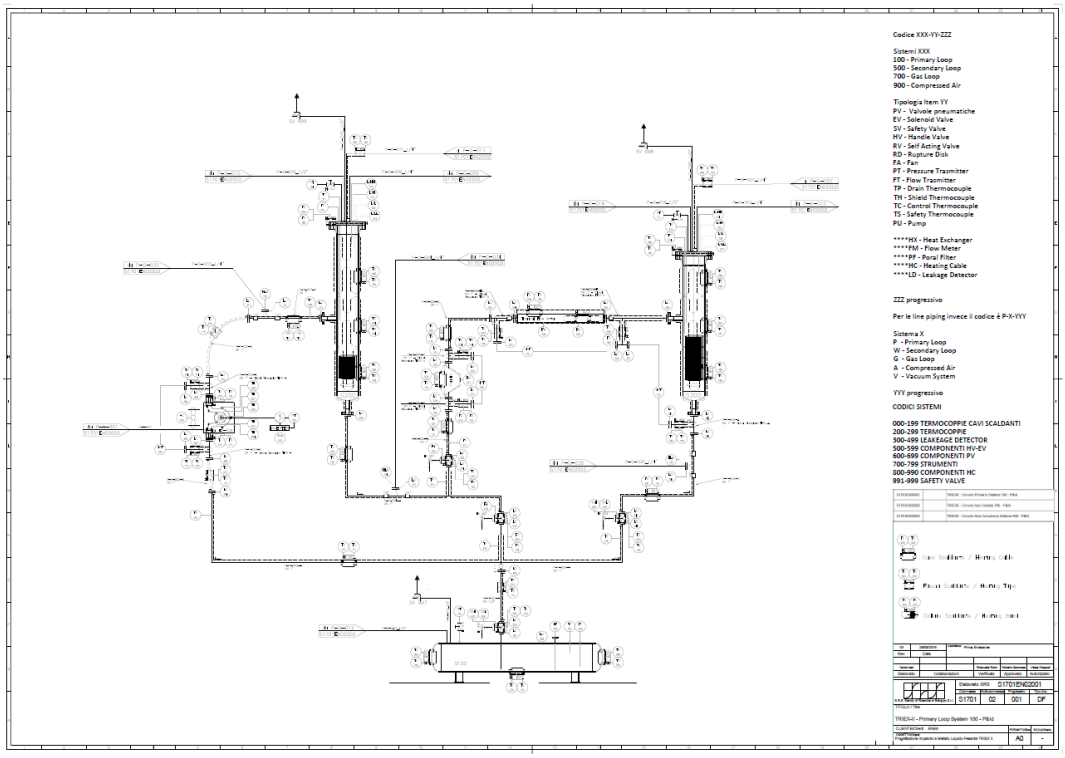

Figure 35 – Lead-lithium loop P&ID of TRIEX II

The main components are presented in detail in the following subsections.

Storage tank S100

This component has the function of storing the eutectic alloy Pb-15.7Li and is kept over 235 °C, fusion temperature of the lead-lithium. It has also the function of draining tank when the plant is not in operation. It is oversized respect to the maximum capacity of the loop, in order to have renewed lead-lithium available and avoid the use of the more superficial layer that could present some impurities (the PbLi is pumped from the bottom of the tank). Figure 36 shows the design of S100. Multiple penetrations are present to install the instrumentations, such as a level

meter, a pressure transducer in gas phase, two thermocouples (one for gas and one for PbLi) and one high-pressure valve. The other penetrations are for the load/discharge of inert gas and to load PbLi in the plant. The main parameters of S100 are presented in Table 13 [64].

Table 13 - Design parameters of S100 of TRIEX II

Parameter	**Value**	**U.o.M.**
Operative temperature	450	[°C]
Design temperature	530	[°C]
Operative pressure	5	[barg]
Design pressure	10	[barg]
Material	2 ¼ Cr-1 Mo	
Total volume	400	[l]
Empty weight	400	[kg]

The material is an alloy resistant to corrosion of liquid lead-lithium. The operative temperature is reached thanks to heating cables all around the metallic shell (Figure 37) and they are controlled from the synoptic. The lead-lithium is pumped from the bottom thanks to the pressure of the cover gas inserted from the top. The conduit connected to the rest of the plant is 20 mm detached from the bottom of S100.

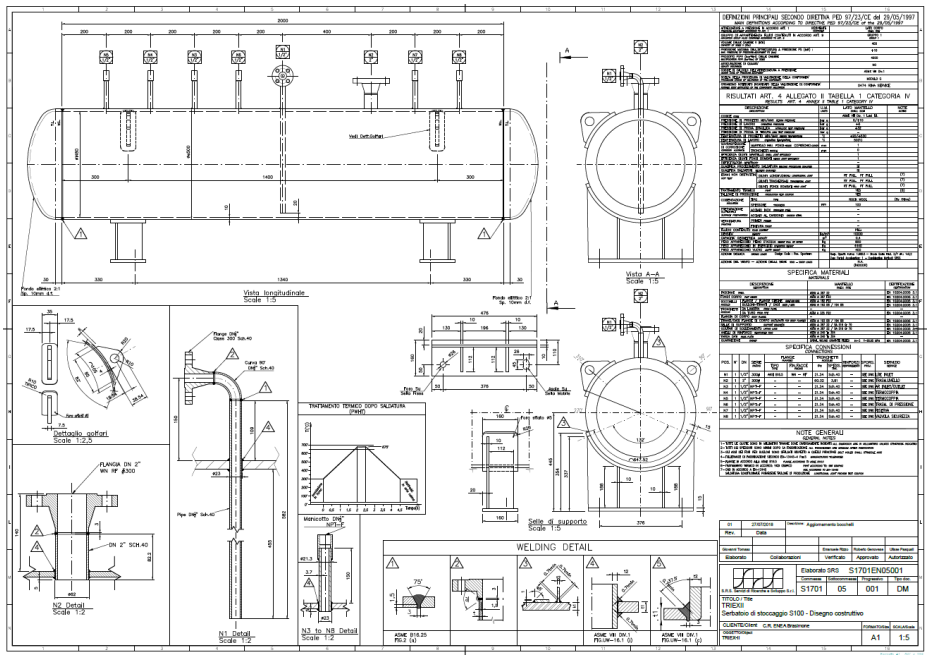

Figure 36 - Storage tank S100 constructive design.

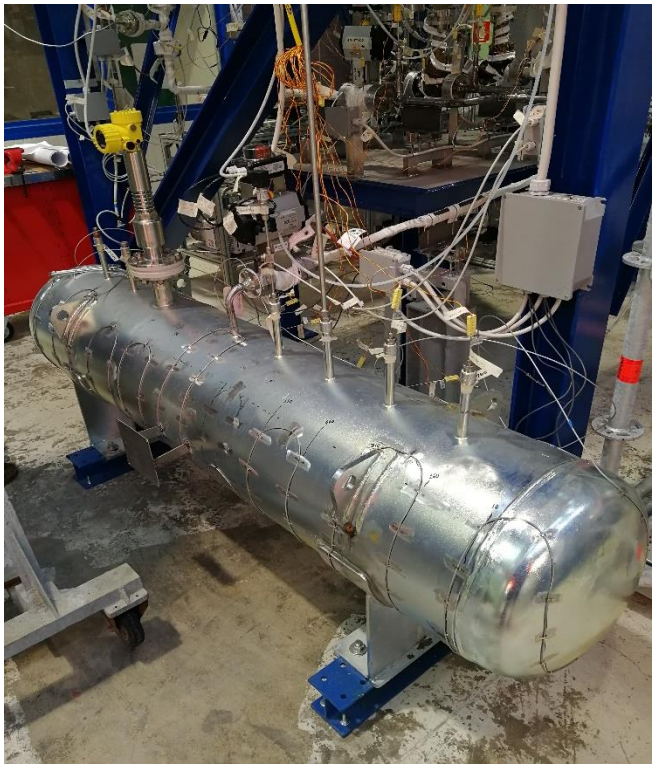

Figure 37 - Picture of S100 storage tank of TRIEX II with heating cables and all the instrumentation installed.

Permanent magnet pump EP100

The permanent magnet pump (Figure 38) is supplied from SAAS GmbH. It must operate at a maximum temperature of 530 °C and the maximum flow rate is 5 kg/s, much higher than the highest value expected in the test matrix. The maximum speed is 700 rpm and is controlled from the DACS with all the security equipment [64]. The channel of the pump is preheated over 250 °C in order to avoid the freezing of the metal during the load of the plant. To reach and maintain this condition the rotation of the pump must be kept at 60-70% of its maximum rotation speed. All the detailed operative conditions are shown in Table 14.

Figure 38 - Permanent magnet pump installed on TRIEX-II.

Table 14 - Operative conditions of the pump [64].

Parameter	Value	U.o.M.
Temperature range	250 - 530	[°C]
Maximum head	4	[bar]
Minimum head	0.3	[bar]
Minimum mass flow rate	0.4	[kg/s]
Maximum mass flow rate	5	[kg/s]
Electrical motor	5,5 kW/400 Vac	
Design pressure	10	[bar]

Saturator S200

The saturator S200 has the same function of the one in TRIEX, solubilize the hydrogen or deuterium in the lithium-lead. It has two modules of packing material and the rest of the height works as a bubble column. The PbLi enters from the middle of the column, because the upper part is used as an expansion volume for the loop to compensate the variations of pressure and level of PbLi. The exit is at the bottom connected to the elliptical dome. Moreover, four level meters are present in order to know the height of the PbLi during operation. On the top of the column there is the gas load/discharge line and the injection system for the tests, that is a 1/4" steel pipe that goes down through all the height and flux the gas at the bottom where is placed a gas distributor. There is also a pressure transducer, a high-pressure valve and two thermocouples that penetrate the dome to read the temperature of the liquid alloy. In Table 15 are presented the operative conditions of the saturator [64].

Table 15 - Operative conditions of the saturator S200.

Parameter	Value	U.o.M.
Design pressure	10	[barg]
Operative pressure	5	[barg]
Design temperature	530	[°C]
Operative temperature	450	[°C]
PbLi mass flow rate	0.2 - 1.2	[kg/s]
Gas flow rate	10 – 250	[Nl/h]
H_2 flow rate	0 – 5	[Nl/h]
Saturation gas	He+H_2 or He+D_2	
Gas injection pressure	2 – 3	[barg]
Maximum concentration H_2	5	[%]
Material	2 ¼ Cr-1 Mo	
Total volume	90	[l]
Empty weight	360	[kg]

In Figure 39, it is possible to see a picture of S200 before the positioning on the structure of TRIEX-II facility.

Figure 39 - Saturator S200 before the installation. The oxide layer is due to the heat treatment applied.

Extractor S300

The extractor column is very similar to S200, but it is smaller with a lower height because has not the function of expansion volume. It has the same instrumentation installed at the top and inside has 4 modules of packing material, Sulzer Mellapak 452Y, shown in Figure 40. The structured packing enhances the contact between gas and liquid phase and slow down the fall of PbLi from the top.

Figure 40 - Mellapak 452Y made of AISI steel 316L in corrugated sheets shape [65].

As explained in section 4.1, GLC packed column relies on the highest possible contact surface in order to maximize the solute exchange. The purging gas He is flow in counterflow from the bottom (as in S200) to extract the hydrogen dissolved. In Figure 41, it is possible to see the constructive design of S300 with details of connection and flanges. As for S200, four level meters are present also in the extractor.

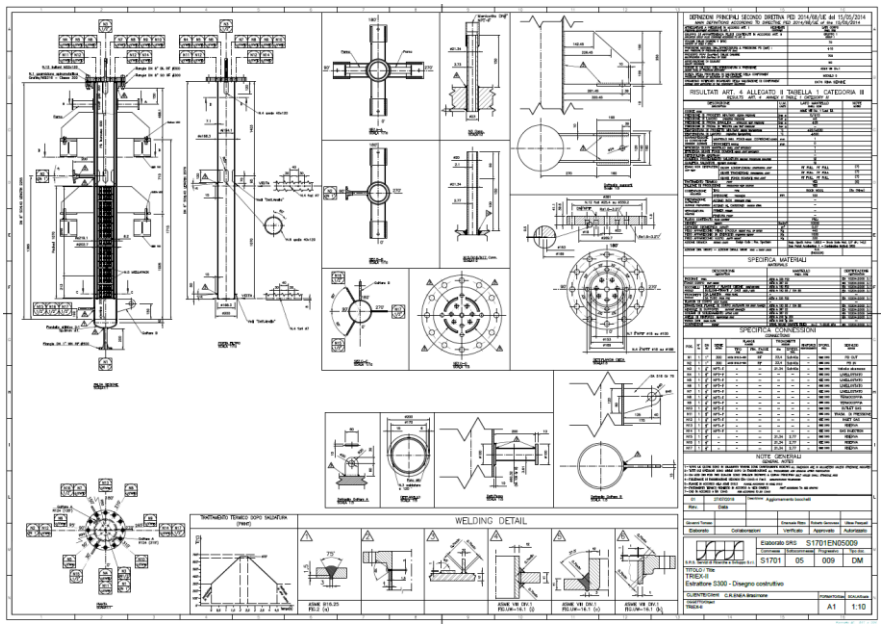

Figure 41 - Extractor S300 constructive design

In Table 16, the operative conditions of the extractor are present [64].

Table 16 - Extractor S300 operative conditions.

Parameter	**Value**	**U.o.M.**
Design pressure	10	[barg]
Operative pressure	5	[barg]
Design temperature	530	[°C]
Operative temperature	450	[°C]
PbLi mass flow rate	0.2 - 1.2	[kg/s]
Gas flow rate	10 - 250	[Nl/h]
H_2 flow rate	0 - 5	[Nl/h]
Extraction gas	He or He+H_2	
Mellapak packing factor	450	[m^2/m^3]
Gas injection pressure	2 - 3	[barg]
Material	2 ¼ Cr-1 Mo	
Total volume	70	[l]
Empty weight	330	[kg]

Other instrumentation

Other instruments are installed in lead-lithium loop to provide the optimal operative conditions and for security reasons:

- *Permeation sensors*: three permeation sensors are present, as in TRIEX, and they are installed at inlet and outlet of S200 and outlet of S300. Differently from the older ones, these sensors have helicoidal shape in order to maximize the surface/volume ratio, one of the parameters that influences the permeation flux through a membrane. Their performances have been tested in Hyper-Quarch as described in section 3.2. They are installed in a cone shaped connection between two flanges. The PbLi floods this cavity and the sensor is immersed in the liquid. After a short pipe stretch outside the upper flange, there is a pressure transducer to read the partial pressure of the hydrogen that is permeated through the iron of the sensor.

- *Thermal flow meter*: the TFM is installed on the inlet pipe of the extractor and it has the function to measure the PbLi mass flow rate. It provides a known heating power to the liquid and measures the different temperature at inlet and outlet of the heating stretch. With these data it is simple to compute the mass flow rate making a simple power balance.

- *Differential pressure transducer*: they are installed to measure the load losses across the pump, the thermal flow meter and the extractor. They are used also for the characterisation of the pump at the operative conditions of the facility.

- *Penetration thermocouples*: placed in different points of the loop to measure the PbLi temperature.

4.3.2 Gas circuit

The gas circuit of TRIEX II is quite more complex than the one of its predecessor. Its function is to provide and discharge the gas to the facility in the correct way and to analyse it. A schematic view can be seen in the P&ID in Figure 42.

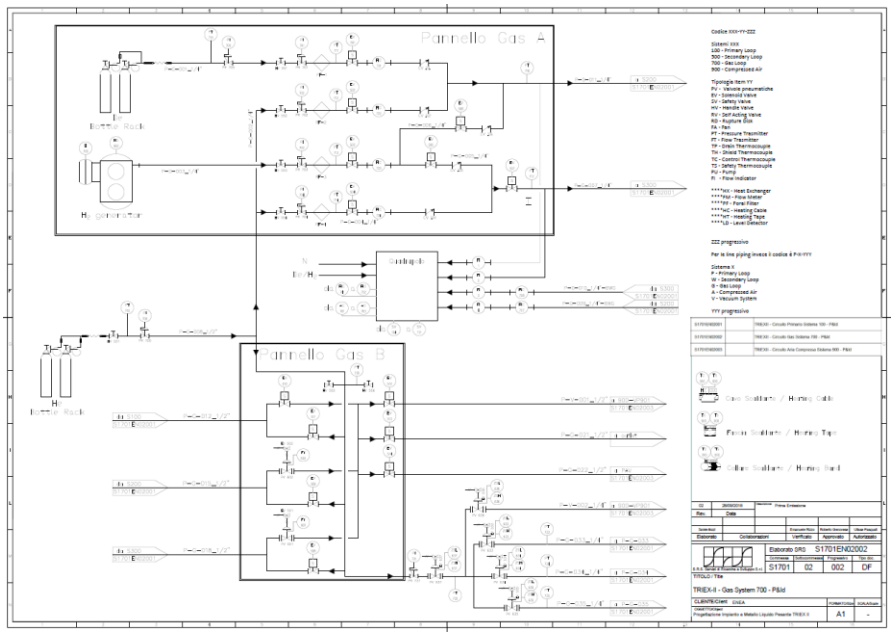

Figure 42 - Gas circuit P&ID of TRIEX II.

There are three main components in this loop: skid A, skid B and the gas analyser.

Skid A

The panel A is the one directly connected to the gas analyser and the lines of inflow and outflow gas to and from S200 and S300 used during the tests are installed here. A picture of the skid can be seen in Figure 43.

Figure 43 - Skid A of the gas circuit.

Helium has two dedicated lines, one for S200 and one for S300 with two different mass flow controllers (MFCs). Another line is for hydrogen, with one MFC that work with lower flow rates and is connected both to S200 and S300. The fourth line is for deuterium, connected only to S200 for the saturation of the last tests in operational mode B. On the right side of the skid, there are multiple penetrations connected to gas analyser that provide the bleed rate of gas to the instrument. On this panel, it is present the DCU that shows the value of pressure of the three permeation sensors and the vacuum degree reached by the two pumps on skid B.

Skid B

The second panel is provided with the load and discharge lines of helium for the three main components of the plant (storage tank, saturator and extractor) and two vacuum pumps are present. A picture of skid B can be seen in Figure 44.

Figure 44 - Skid B of gas system. The vacuum pumps are positioned on the lower work plan.

There are three valves to load He in the plant and three valves to discharge gas from S100, S200 and S300. They are all connected to 1/2-inch pipes. The load line comes from the reservoir of He installed outside and the discharge one goes outside to an external tank. On the work plane, there is a rotary

vane vacuum pump, provided by Edwards, connected to the load/discharge line that is used to make the vacuum in the lead-lithium loop in order to remove possible air or other impurities that could be present. The other pump is a diaphragm-turbomolecular pump, provided by Pfeiffer, and is used to make the vacuum in the permeation sensor's line, that have an isolated circuit in order to avoid contamination from impurities. The sensor's line is also connected to He in order to make a slight overpressure if needed.

Gas analyser

The gas analyser comes from ESS Ltd and it is an ESSCO GeneSys 200D model. The technical specifications of the instrument are shown in Table 17.

Table 17 - Technical specifications of GeneSys 200D.

Parameter	**Value**	**U.o.M.**
Mass analyser	Quadrupole	
Detector	Dual Faraday/Channeltron	
Power	170	[W]
Pumping system	TMP + scroll pump	
Gas intake system	No. 2 capillaries of 2 m heated silicon	
Inlet gas pressure	750-1500	[mbar]
Inlet gas temperature	200 - 350	[°C]
Consumption at the capillary	10-20	[sccm]
Mass detection	1 - 100 (200 standard)	[amu]
Limit of detection (LOD)	1	[ppb]
Response analysis time	120	[ms]
Precision	+/- 5	[%]

It has six sample lines: four of them are connected to the plant and two are used for calibration and background of the instrument. The first four lines sample the gas respectively from injection line of saturator and extractor and from outlet gas line of saturator and extractor (they are called S1, S2, S3 and S4). There are also four manual flow controllers to set a proper gas flux that enters inside the instrument. All the six lines are controlled by the software and are intercepted by six different valves that are normally

closed. Before the beginning of the experimental campaign the calibration of the instrument is needed. This procedure is used to set the spectrometer for the analysis of gas mixtures used during the tests. In fact, it is performed with two cylinders, one with a mixture of $He+H_2$ and one with $He+D_2$, both with known concentrations of the different species. Moreover, there is the background procedure. The background procedure serves to improve the calibration and to remove from the data analysis the residuals inside the instrument that could accumulate in time. It is optional and should be done before the calibration in order to have more accurate readings. The spectrometer is equipped with two RF generators that are suitable for readings in two distinct range of atomic mass of the gas analysed. One works from 1 to 5 amu, used to distinguish He (4 amu) from D_2 (4,027 amu), and the other from 1 to 200 amu, for a wider range of inspection. In Figure 45 can be seen a picture of the spectrometer with the two RF generators on top.

Figure 45 - ESSCO GeneSys 200D.

The detection of the sample gas is done through a Faraday detector and a SEM multiplier, that supply high voltage signal. The vacuum inside the analysing chamber can reach a value of $10^{-7}/10^{-8}$ mbar. In order to avoid formation of water, due to possible humidity in the room, heaters are

installed and can be switched on/off from the frontal panel of the spectrometer.

From the software point of view, multiple visualization and analysis options are possible. The Analogue tab (Figure 46) is an analogical scan of the actual sample gas and peaks of the present species can be seen.

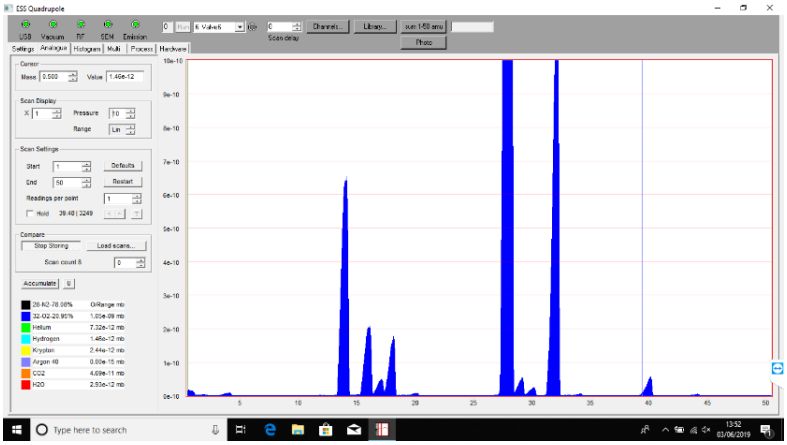

Figure 46 - Example of analogue spectrum. In this case the gas is air.

In this tab, it is possible to see more in detail the composition of a certain sample. Instead, in the Multi tab Figure 47 the concentrations in time can be seen and are plotted. They can be also saved and further analysed.

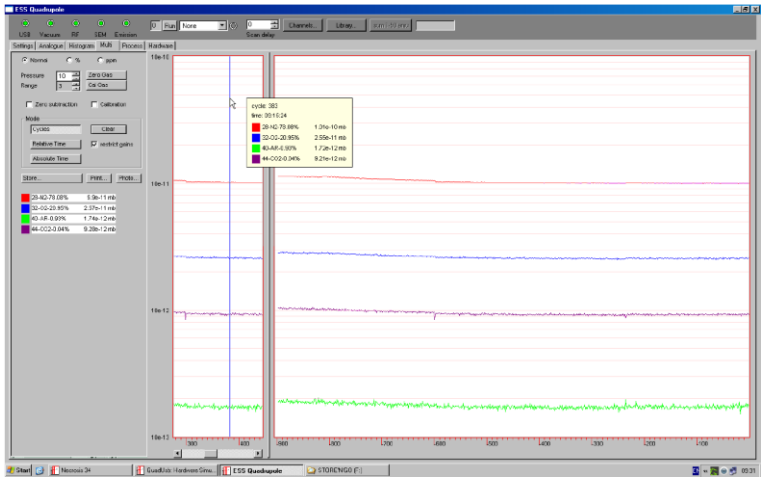

Figure 47 - Multi tab of the software where the trend in time can be seen. The example is with air.

In this panel the calibration and background procedures can be done.

5 Model and results

Before starting the experimental campaign on TRIEX-II facility, preliminary calculations and modelling have been done. A model of all the lead-lithium loop has been developed to have a mass balance of the system and a computation of the permeation fluxes through the pipes.

5.1 0D model for TRIEX-II: mass balance of the system

A 0D model for TRIEX-II liquid metal loop has been developed with Matlab/Simulink software [66]. The aim of the work is to develop a model that could be also used to compare the experimental extraction efficiency with the theoretical one, keeping into account multiple factors that could affect it in all the circuit. A mass balance equation has been written for each main component (section 4.3), each considered as a subsystem in Simulink environment. Only the circuit section interested during the tests has been considered, so that the storage tank S100 and the pipe stretch for the loading of the lithium-lead were not considered. For pipes, Eq. (5.1) has been written. The unknown variable is the concentration of hydrogen in PbLi at the exit of the component.

$$V_p \frac{dC_{H,out}}{dt} = Q_{PbLi,p}\left(C_{H,in} - C_{H,out}\right) - \frac{\phi_p A_{lat,p}}{th_p}\sqrt{p_{H,in}} \tag{5.1}$$

where V_p [m^3] is the internal volume of the pipe, $C_{H,in}$ [mol/m^3] and $C_{H,out}$ [mol/m^3] are hydrogen concentration in PbLi at the inlet and the outlet respectively, $Q_{PbLi,p}$ [m^3/s] is the lithium-lead volumetric flow rate for that pipe section, ϕ_p [$mol/m/s/Pa^{0.5}$] is the permeability of the pipe's steel, $A_{lat,p}$ [m^2] is the lateral surface of the pipe, th_p [m] is the thickness of the pipe and $p_{H,in}$ [Pa] is the is the partial pressure of hydrogen in PbLi at the inlet. The partial pressure of hydrogen in PbLi is calculated through the Sieverts' law. To calculate the permeation flux, the inlet pressure has been considered, to be more conservative because it is the highest value of pressure in this component. The permeation flux through the pipe has been written following the Richardson's equation and considering null the partial pressure of hydrogen in the outer environment. For the calculations,

the permeability of EUROFER 97 has been taken for all the steel components. This is due to the fact that the real value of solubility for steel A 182 Gr F22, the material of piping, has not been found in literature and the one of EUROFER has been chosen as approximation because they are both ferritic-martensitic steels. Eq. (5.1) has been applied for four pipe traits:

- From saturator S200 to extractor S300;
- From saturator S200 to the end of the by-pass line;
- From extractor S300 to saturator S200;
- From saturator S200 and return to S200 (when only saturation occurs);

The total length of the pipes considered in the model is higher than the real one for having a conservative calculation, considering a higher permeation surface.

The saturator S200 has been implemented with a similar mass balance equation with the addition of a source term:

$$V_S \frac{dC_{H,out}}{dt} = Q_{PbLi,S}\left(C_{H,in} - C_{H,out}\right) - \frac{\phi_S A_{lat,S200}}{th_{S200}}\sqrt{p_{H,out}} + S \qquad (5.2)$$

where V_S [m^3] is the internal volume of the saturator filled with PbLi and S [mol/s] is the source term, described in Eq. (5.3):

$$S = Q_{gas,S}\left(C_{H_2,gas,in} - C_{H,in}\right) \qquad (5.3)$$

where $Q_{gas,S}$ [m^3/s] is the volumetric flow rate of gas injected into the the saturator and $C_{H_2,gas,in}$ [mol/m^3] is the concentration of hydrogen in the gas mixture injected into the saturator. The source term will tend to zero gradually until the complete saturation of lithium-lead.

The extractor S300 has been implemented with the same form of Eq. (5.2):

$$V_E \frac{dC_{H,out}}{dt} = Q_{PbLi,E}\left(C_{H,in} - C_{H,out}\right) - \frac{\phi_E A_{lat,E}}{th_E}\sqrt{p_{H,out}} - E \qquad (5.4)$$

where E [mol/s] is the extraction term. This has been implemented as in Eq. (5.5):

$$E = Q_{gas,E}\, C_{H,in} \tag{5.5}$$

where $Q_{gas,E}$ [m^3/s] is the volumetric flow rate of gas injected for the extraction. The extraction term will tend to zero until the concentration of hydrogen will be null. The operation mode of the experiment expects the simultaneous functioning of the saturator and the extractor, trying to reach an equilibrium between the hydrogen extracted and the solubilized one. This is the reason of the implementation also of the by-pass section and why the lithium-lead flow rates in S200 and S300 have been distinguished in two variables.

All these equations have been implemented in multiple subsystems that can be seen assembled in Figure 48. The blocks used for the solution of the differential equations in one subsystem are shown in Figure 49.

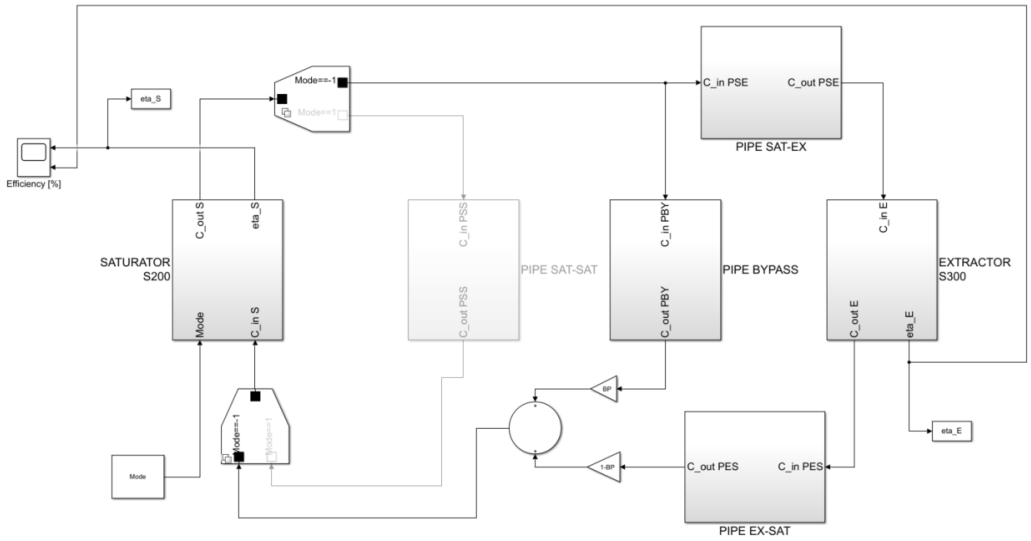

Figure 48 - Simulink 0D model for TRIEX-II system balance.

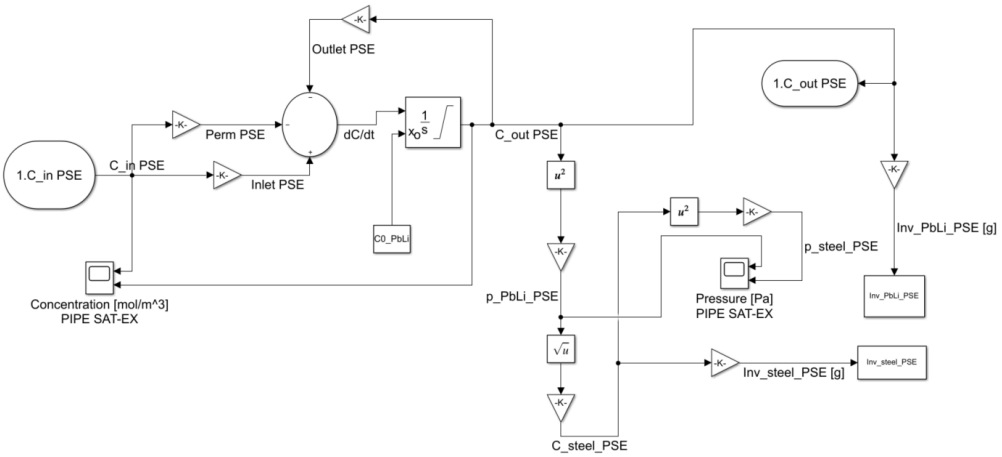

Figure 49 - Internal blocks of a subsystem of the Simulink 0D model.

This 0D model has been adapted to the tests carried out on TRIEX-II facility doing a benchmark between the theoretical and experimental results.

5.2 Coupling between Simulink and COMSOL Multiphysics

The saturator and the extractor are the bigger parts of the lead-lithium loop and considering them as 0D components could be a too strong approximation. A 2D model for S300 has been built with COMSOL Multiphysics considering also the fluid dynamics of PbLi inside the component with the Mellapak installed. Thanks to the COMSOL Multiphysics Livelink for Matlab tool, it is possible to do the implementation of the two models. For doing this, a suitable S-function must be written in Matlab environment [67]. The working principle of the S-function developed in Simulink is shown in Figure 50.

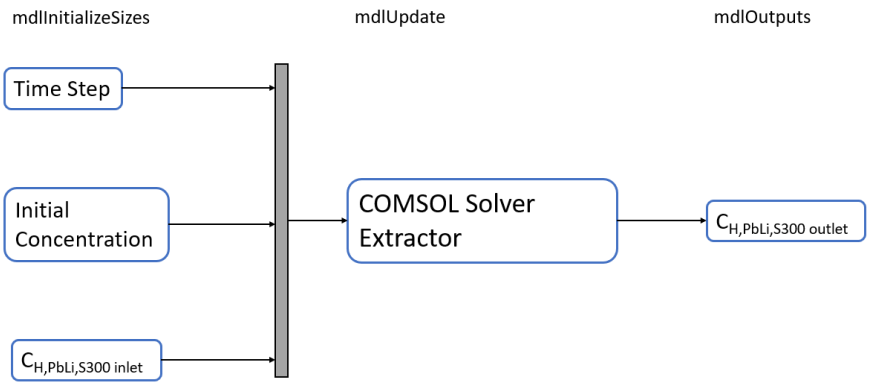

Figure 50 - Simulink S-function for the extractor.

The S-function blocks will replace the subsystem blocks of the saturator and the extractor of the 0D model. The purpose of the S-function is to "call" the COMSOL solver to solve the turbulent flow and transport physics in the Simulink environment, without using the graphics interface of COMSOL. Simulink provides the time variable and the input for the 2D solver. In this case, the input variable is the concentration of hydrogen evaluated at the output of the pipe that comes before the extractor or the saturator. The coupled model Simulink/COMSOL is shown in Figure 51.

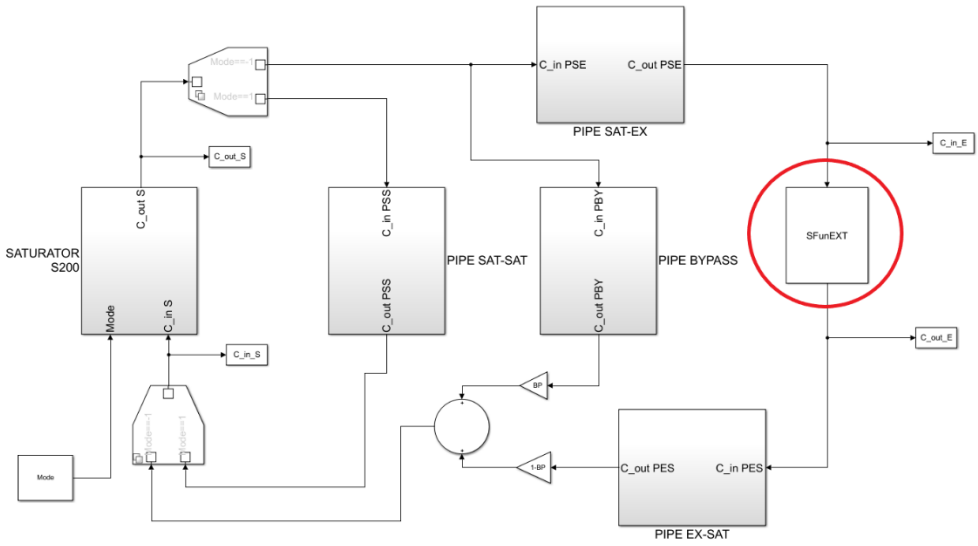

Figure 51 - Layout of the coupled Simulink-COMSOL models. The S-function block is highlighted with a red circle.

As first step, Simulink initializes the model creating and loading the variables needed for the S-function [67]. In the initialization the COMSOL model is loaded with all the characteristics and features that would appear in the model tree in COMSOL graphical interface. The timestep chosen for the solver is fixed at 30 s because it is the minimum value that gives satisfying results in the 0D model, so that the same timestep has been kept also for the coupling.

The second step is the update of the simulation. In this phase, the COMSOL solver is run at each timestep updating the condition of calculation. The input concentration is set as initial condition all over the domain of lithium lead at each update. In fact, the solver is set to do computations always from zero to 30 s, using as initial condition the updated concentration in the loop

thanks to the 0D blocks of Simulink. Finally, the output is calculated as the mean concentration over lithium-lead domain and used as input in the block that represents the pipe section after the saturator or the extractor.

As first try, only the extractor's S-function has been implemented because of the large time required for the software to solve the model.

5.3 Experimental results and analysis

The experimental campaign on TRIEX-II facility has been carried out from mid-April to mid-June 2019 [37]. For the operational mode A, 19 tests have been done and for the operational mode B with deuterium 6 tests have been carried out.

5.3.1 Operational mode A: tests with H_2

For the tests in operational mode A, hydrogen has been solubilized in lithium-lead before starting the campaign. The solubilized concentrations are of the order of magnitude interesting for the ITER TBM design. The temperature of the tests has been varied from 400 °C to 450 °C to see the behaviour of the extraction efficiency as function of temperature. The lead-lithium is kept at constant temperature during each test. The range of the parameters in op. mode A is shown in Table 18.

Table 18 - Parameters of operational mode A [37].

Parameters	**Value**	**U.o.M.**
Nominal Pb-15.7Li mass flow rate	0.2 ÷ 1.2	[kg/s]
Saturator S200 gas flow rate	10 – 100	[Nl/h]
Saturator gas inlet composition	He+H_2 (5% max.)	
Max. H_2 concentration in S200 gas inlet	5	[vol. %]
Gas pressure at S200 inlet	2 ÷ 4	bar
Purge gas for S300 inlet	He	
Extractor gas flow rate	50-450	[Nl/h]
Purge gas composition at S300 outlet	He+H_2 (500 ÷ 2000 vppm)	
H_2 partial pressure range	70 – 180	[Pa]
Purge gas pressure at S300 inlet	2 ÷ 4	bar

Determination of the efficiency with the permeation sensors and mass spectrometer

The extraction efficiency through permeation sensors is calculated as:

$$\eta = \frac{C_{H,in} - C_{H,out}}{C_{H,in}} = 1 - \frac{C_{H,out}}{C_{H,in}} \tag{5.6}$$

Introducing the Sieverts' law, it yields:

$$\eta = 1 - \frac{K_S\sqrt{p_{out}}}{K_S\sqrt{p_{in}}} = 1 - \sqrt{\frac{p_{out}}{p_{in}}} \tag{5.7}$$

In this way, the efficiency is computed without using the Sieverts' constant and it depends only on the partial pressure read by the permeation sensors HLM734 and HLM735. The accuracy of this method is linked to the accuracy of the readings of the two permeation sensors.

Another way to evaluate the efficiency is using the mass spectrometer. With this instrument is possible to know the concentration of hydrogen in the stripping gas at the outlet and inlet of the extractor and use the mass balance equation for a packed column, Eq. (4.3), to evaluate the molar fractions in the lithium-lead:

$$x_{out} = x_{in} - 2\,\frac{G_M}{L_M}\,(y_{out} - y_{in}) \tag{5.8}$$

where x_{in} and x_{out} are the molar fraction of the hydrogen in PbLi at the inlet and outlet of the extractor, respectively, G_M [mol/s] is the molar flow rate of stripping gas, L_M [mol/s] is the molar flow rate of PbLi and y_{out} and y_{in} are the hydrogen molar fraction in the stripping gas at the outlet and the inlet of the extractor, respectively. In this case, y_{in} is zero because pure helium is injected into the extractor as purge gas.

To evaluate the inlet molar fraction in PbLi, the values of partial pressure measured by HLM734 are used. From this, x_{in} can be calculated as:

$$x_{in} = K_S \cdot \sqrt{p_{H_2,in}} \cdot \frac{PM_{PbLi}}{\rho_{PbLi}} \tag{5.9}$$

where $p_{H_2,in}$ [Pa] is the hydrogen partial pressure read by HLM734, PM_{PbLi} [kg/mol] is the molecular weight of the liquid metal and ρ_{PbLi} [kg/m3] is the lithium-lead density. Combining Eqs. (5.8, 5.9), it yields:

$$\eta = \frac{2\,\rho_{PbLi}}{K_S\,\sqrt{p_{H_2,in}}\,PM_{PbLi}}\,\frac{y_{out}-y_{in}}{L_M/G_M} \tag{5.10}$$

The efficiency is expected to increase when the L_M/G_M ratio decreases, for example increasing the molar gas flow rate or decreasing the molar lithium-lead flow rate. This method requires the information of the partial pressures, so that the accuracy of the results depends also on one permeation sensor precision. The other instrument involved is the gas analyser, but it has been seen in section 4.3.2 that the accuracy of this instrument is very high and it can distinguish the gas species even at low concentrations, so the gas molar fraction measurements should not introduce a sensible error in the result. The parameter that influences strongly the efficiency calculation is the Sieverts' constant for hydrogen in PbLi. The correlations for the solubility are of the Arrhenius type so that depends on the temperature at which the experiments have been done. Three values scattered among two order of magnitude have been taken for the analysis and they are shown in Table 19.

Table 19 - Solubility values from three different authors, evaluated at 400°C.

Parameter	Value at T=400 °C	U.o.M.	Ref.
Reiter solubility	$1.06*10^{-3}$	$[mol/m^3/Pa^{0.5}]$	[43]
Aiello solubility	$2.39*10^{-2}$	$[mol/m^3/Pa^{0.5}]$	[45]
Chan-Veleckis solubility	$5.20*10^{-3}$	$[mol/m^3/Pa^{0.5}]$	[44]

These three different numbers have been used in eq. (5.10).

Experimental results

The results of the tests carried out on TRIEX-II in op. mode A are shown in Table 20.

Table 20 - Experimental results for the operational mode A [37].

TEST #	T [°C]	L [kg/s]	G [Nl/h]	L/G	$p_{H_2,in}$ [Pa]	y_{out} [-]	η_R [%]	η_A [%]	η_{CV} [%]
1	400	1.35	181	2.5	187	6.00E-05	33.2	1.5	6.8
2	400	1.15	192	2.1	115	1.68E-04	154	6.8	31.4
3	400	0.67	128	1.9	177	1.38E-03	1139	50.5	232
4	400	0.66	128	1.9	136	1.35E-03	1255	55.7	255
5	400	1.13	138	3	127	5.00E-05	30.7	1.4	6.2
6	400	0.67	83	3	118	2.00E-05	12.6	0.5	2.6
7	400	0.60	250	0.9	128	3.39E-05	69.6	3.1	14.2
8	400	1.14	243	1.7	116	5.10E-05	48.2	2.1	9.8
9	400	1.15	14	30.3	197	5.10E-05	2.5	0.1	0.5
10	400	0.20	51	1.6	125	4.00E-05	45.5	2	9.3
11	400	0.20	>250	0.3	141	2.28E-04	1267	56.2	258
12	400	0.20	>250	0.3	180	6.30E-05	324	14.4	66
13	450	1.18	90	4.9	115	5.40E-03	2073	79.4	384
14	450	1.20	52	8.6	78	8.60E-04	232	8.9	43
15	450	1.20	209	2.1	125	2.72E-03	2351	90	436
16	450	0.45	55	3	106	1.26E-03	825	36.6	168
17	450	0.55	111	1.8	129	7.23E-04	683	30.3	139
18	450	0.55	207	1	67	7.32E-04	1741	77.3	355
19	450	0.2	100	0.7	100	1.48E-04	405.3	18.0	50.3

where η_R, η_A and η_{CV} are the efficiencies evaluated with Reiter, Aiello and Chan-Veleckis solubilities, respectively. The ratio L/G has been evaluated with the volumetric flow rates of lithium-lead and stripping gas. These results show that in terms of efficiency there is a big discrepancy between the different correlations available in literature for the Sieverts' constant evaluation. Especially, lower is the solubility and higher is the extraction efficiency because it appears at the denominator in eq. (5.10). In some cases, for Reiter and Chan-Veleckis values the efficiency computed is also higher than the unity, because the too low solubility lead to a negative value of the hydrogen molar fraction in PbLi evaluated at the outlet of the extractor column.

The efficiency evaluated with the permeation sensors across the extractor has not been reported because in multiple tests they gave misleading results, that lead to negative extraction efficiencies or almost null values of η. In some cases, the trend over the time of the sensors was not stable

enough to be used for the calculation. Also, the pressure at the outlet of S300 was higher than the one at the inlet, probably due to the fact that some hydrogen was accumulated in the sensors chamber, so that it was necessary to do the vacuum inside the plant to remove all possible gas contaminations.
A positive aspect is an average increase in the efficiency with the raise of the temperature. A higher temperature means higher value of solubility but also an increase in the permeation flux, favouring the hydrogen exchange between lithium-lead and the stripping gas.

Analysis

Few tests have been analysed and a comparison between them and the efficiency calculated with the mass spectrometer has been done. The chosen tests for this comparison are the Test#1 and Test#5. The efficiency evaluated with the sensors HLM734 and HLM735 are reported in Table 21 and the trend of the two sensors can be seen in Figure 52 and Figure 53.

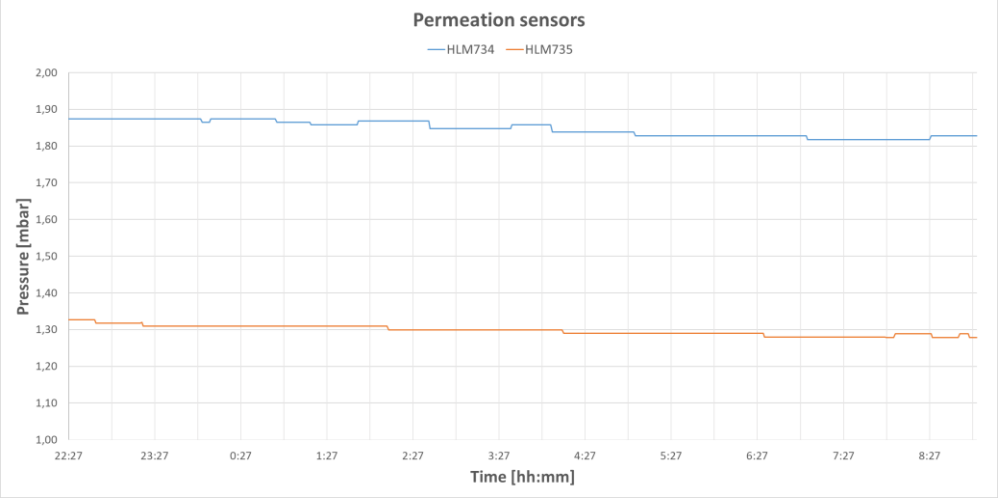

Figure 52 - Permeation sensors trend for Test#1.

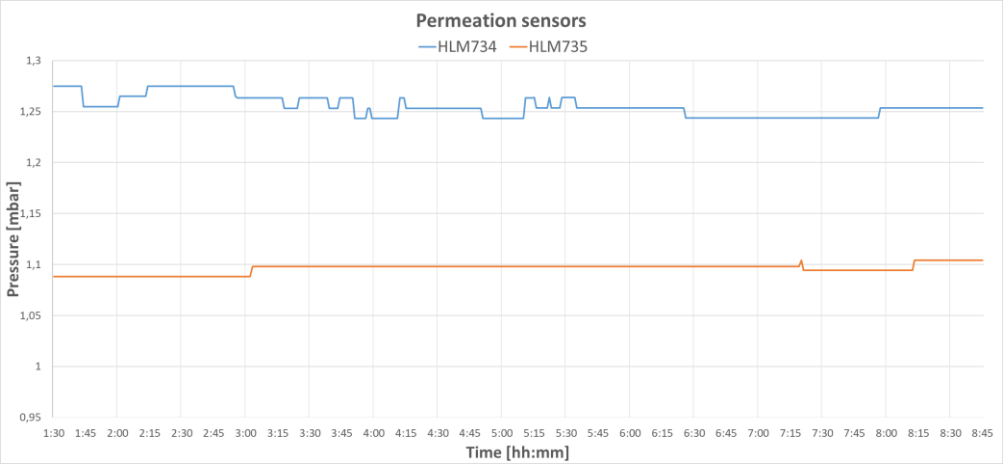

Figure 53 - Permeation sensors trend for Test#5.

The time period chosen for the analysis was the one in which the sensors showed a stable trend during the extraction test, with a net difference between the inlet and the outlet concentration.
Also, the theoretical Sieverts' constants needed to obtain η are shown. The efficiency had been evaluated with eq. (5.10).

Table 21 - Experimental efficiency for the Test#1 and Test#5 evaluated with the sensors [37].

Parameter	**Test#1**	**Test#5**
Experimental efficiency, η [%]	16.2	6.5
Theoretical solubility, $K_{S,exp}$ [mol/m^3/Pa]	3.57*10^{-2}	4.92*10^{-3}
$K_{S,exp}/K_{S,Reiter}$	33.68	4.64
$K_{S,exp}/K_{S,Aiello}$	1.49	0.21
$K_{S,exp}/K_{S,Chan-Veleckis}$	6.87	0.95

The results obtained highlight that the optimal Sieverts' constant values stay above $K_{S,Aiello}$ for the Test#1 and it is very close to $K_{S,Chan-Veleckis}$ for Test#5. The order of magnitude obtained is between 10^{-2} – 10^{-3} [mol/m^3/ Pa$^{0.5}$] as the values found in literature, but a slight difference can lead to significant variation in the final extraction efficiency evaluation, as can be seen in Table 20.

Code benchmark

Among the significative tests, the operating conditions of Test#1 have been inserted as input in the 0D model to do a benchmark between the

code and the experimental results. The obtained concentration of hydrogen at the inlet and the outlet of the extractor are shown in Figure 54.

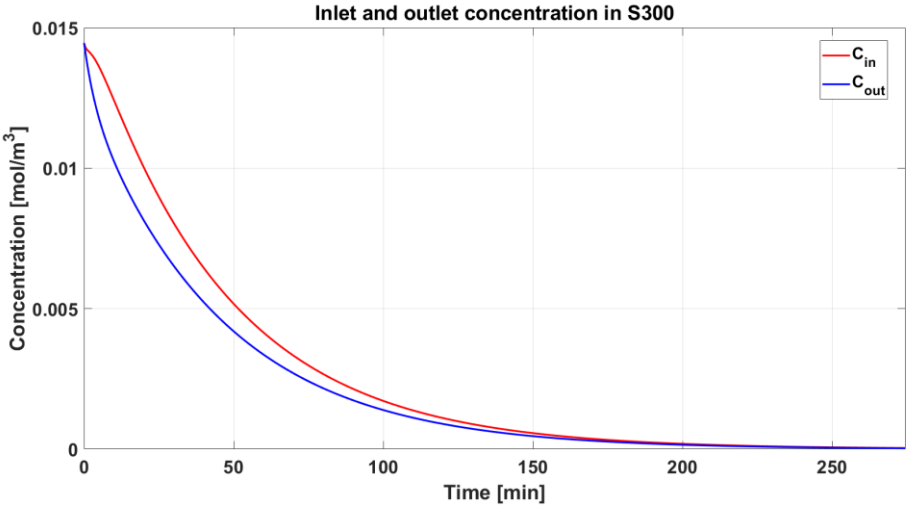

Figure 54 - Concentrations trend over time across the extractor S300.

The test has been carried out keeping close the bypass valve and with no saturation happening in S200 to compensate the hydrogen extracted. Obviously, from a mathematical point of view, without a source of hydrogen the values will tend to zero after some time while this is not happened in the real trend of the permeation sensors HLM734 and HLM735. However, the ratio between the concentrations at the inlet and the outlet of the extractor has remained constants after few timesteps for all the duration of the simulation, as shown in Figure 55.

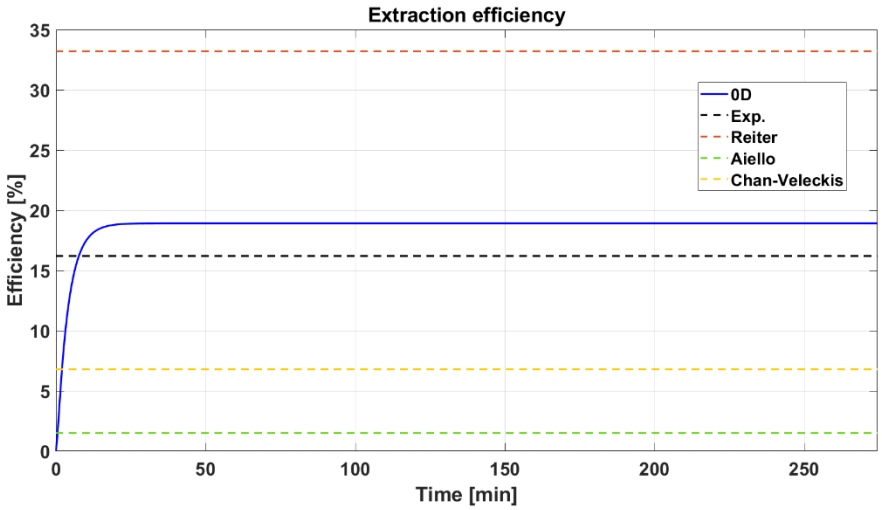

Figure 55 - Comparison of the extraction efficiency in Test#1 between experiments and 0D model.

After few timesteps, the efficiency evaluated with the 0D model is stable and coherent with the one measured with the sensors. The time needed for the stabilization of the system is about 20 minutes and then the extraction efficiency does not change anymore. The deviation from the experimental efficiency has been evaluated with eq. (5.11).

$$err_\eta = \left| \frac{\eta_{exp} - \eta_{0D}}{\eta_{exp}} \right| \cdot 100 = 16.7\ \% \tag{5.11}$$

The efficiencies evaluated with the Reiter Sieverts' constant, the one used in the calculation, is quite different from the one of the model, just like the other two with the other solubility values. This discrepancy could be caused by the strong approximation of the geometry of the system together with the simple mathematical model adopted to describe the extraction term in S300. However, the deviation evaluated between the value measured with the HLM734 and HLM735 and the one computed could lead to the conclusion that the code is good for a first approximation of the lithium-lead loop and a first look to the expected trends of the concentrations and partial pressure of hydrogen dissolved.

Another evaluation was the order of magnitude of the permeation fluxes towards the environment. They have been evaluated with the Richardson's equation and their trend is shown in Figure 56.

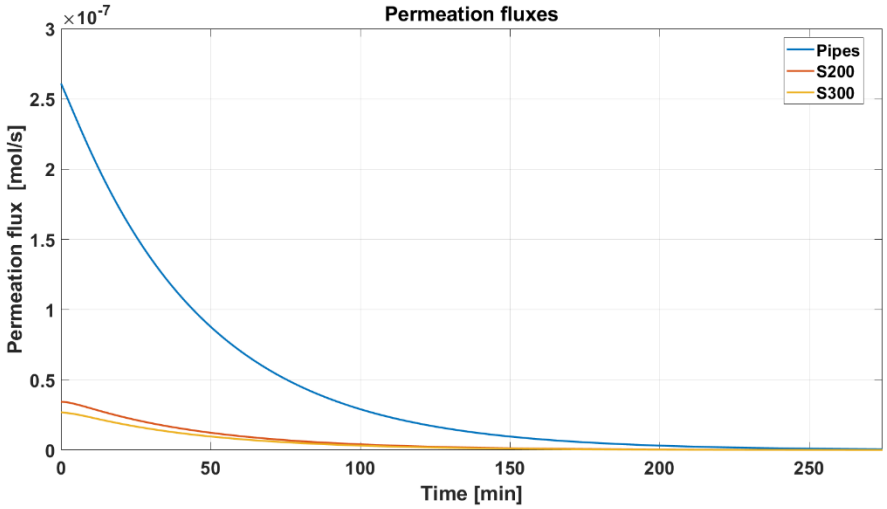

Figure 56 - Permeation fluxes through pipes, saturator and extractor.

As for the concentrations, the final value tends to zero. The main difference is between the permeation flux of the pipes and the one of S200 and S300.

There is an order of magnitude of difference between them, considering that the thickness of the steel of the extractor and the saturator is higher than the one of the pipes. The maximum values for t=0 are shown in Table 22.

Table 22 - Permeation fluxes maximum values at t=0 s.

Parameters	Value	U.o.M.
Pipes permeation flux	$2..61*10^{-7}$	[mol/s]
Saturator permeation flux	$3..44*10^{-8}$	[mol/s]
Extractor permeation flux	$2.71*10^{-8}$	[mol/s]
Total permeation flux	$3.23*10^{-7}$	[mol/s]

Considering the sum of all the values and supposing to have tritium instead of hydrogen, almost twelve days are required to release 1 g of substance in the environment. The calculation has been done with the maximum value of permeation flux, so that we are very conservative. This evaluation lead to the conclusion that the permeation fluxes towards the external environment are negligible respect to the moles of hydrogen involved in the extraction process and that are dissolved in lithium-lead.

5.3.2 Operational mode B: tests with D_2

In the operational mode B, deuterium has been solubilized in lithium-lead after the removal of all the residual hydrogen (this procedure took about 3-4 days). The composition of the stripping gas is $He+H_2$ so that at the outlet of the extractor the in the gas analyser are found traces of HD and D_2 together with H_2, that has not been solubilize in the PbLi. For this operational mode the mass spectrometer has been recalibrated and switched to the RF 1-5 amu, in order to be able to distinguish between He and D_2. The main parameters for op. mode B are shown in Table 23.

Table 23 - Operating conditions for op. mode B [37].

Parameters	Value	U.o.M.
Nominal Pb-15.7Li mass flow rate	0.6 ÷ 1.2	[kg/s]
Saturator S200 gas flow rate	10 – 100	[Nl/h]
Saturator gas inlet composition	$He+D_2$ (5% max.)	
Max. H_2 concentration in S200 gas inlet	5	[vol. %]

Gas pressure at S200 inlet	2 ÷ 4	bar
Purge gas for S300 inlet	He+H_2 (0.5% max)	
Extractor gas flow rate	50 – 450	[Nl/h]
Purge gas composition at S300 outlet	He+H_2 (10000 ÷ 50000 vppm) + He+HD (1 – 100 vppm)	
H_2 partial pressure range	70 – 180	[Pa]
Purge gas pressure at S300 inlet	2 ÷ 4	bar

Experimental results

With deuterium 6 tests have been carried out, all at 450 °C because of the higher efficiency seen at higher temperatures. The results obtained with deuterium test are shown in Table 24.

Table 24 - Tests results of operational mode B with deuterium [37].

TEST #	T [°C]	L [kg/s]	G [Nl/h]	L/G	$p_{H,in}$ [Pa]	$y_{out}[\frac{\mathbf{vol}_{D_2}}{\mathbf{vol}_{\mathbf{out,gas}}}]$	Extraction flux HD+D2 [Nl/h]
1	450	0,6	50	4,5	135	2,47E-02	1,24E+00
2	450	0,6	103	2,2	140	2,49E-02	2,56E+00
3	450	0,95	52	6,8	146	2,45E-02	1,27E+00
4	450	0,2	50	1,42	152	2,67E-02	1,34E+00
5	450	1	50	7,34	179,5	2,00E-02	1,00E+00
6	450	0,5	30	6,6	1,69	2,17E-02	6,51E-01

The results obtained show a higher fraction of solubilized gas removed with an extraction flux of HD+D_2 higher than the one in operational mode A tests. A relevant part of deuterium is removed through HD molecule that is easier to distinguish from He respect to pure deuterium. Unfortunately, it was not possible to evaluate the extraction efficiency with the permeation sensors because 0.5% of hydrogen was used in the stripping gas and a part has been solubilized in the lithium-lead and measured by the sensors, giving a false partial pressure combination of hydrogen and deuterium that have permeated through the iron membrane.

Facility criticalities

Multiple criticalities have been found during the experimental campaign carried out on TRIEX-II and hereafter listed [37]:

- Only for some tests it was possible to have a stable value of the trend of the hydrogen permeation sensors during the tests. The hydrogen permeation sensors are stabilized at the beginning of each test giving the x_{in} value, but especially with high purge gas flow rates, the pressure inside the sensors increased continuously after the extraction starting and sometimes the tests have been stopped and repeated. Probably, helium bubbles were trapped by liquid metal flow and release inside the hydrogen permeation sensor box so that the hydrogen concentration measured by permeation sensor is due to the accumulation of gas that increased the pressure inside the probe box;
- It has been found that the hydrogen partial pressure measured by permeation sensor is correlated to PbLi pressure, therefore the hydrostatic pressure plays a role in the measure;
- The literature values of Sieverts' constant of hydrogen solubilized in PbLi have been found to be not compatible with the pressure trends obtained, indicating a deviation from literature values up to one order of magnitude. The efficiencies evaluated are strongly scattered between very low values and other with no physical meaning;
- At high PbLi mass flow and low stripping gas flow the GLC efficiency was very low. Probably this is due to the fact that the lithium-lead entrains the gas without allowing it a uniform distribution along the extractor height.

6 Conclusions

Several steps have been done in the roadmaps that will lead to the first fusion reaction in ITER and the first kilowatt production with DEMO reactor. The WCLL TBM concepts will be tested in ITER in order to characterise the tritium breeding and removal processes. Two main aspects relative to this last purpose have been analysed in this work: a suitable way to measure hydrogen concentration in lithium-lead and the extraction efficiency with a GLC packed column.

The permeation sensors were developed in a previous experimental campaign, testing different materials and identifying the criteria needed for an optimal material and design. Two solutions have been tested in Hyper-Quarch device, a cylindrical and a helical iron sensor, both in gas phase and liquid phase and in equilibrium mode. The time needed for the stabilization were quite high, of the order of several hours, and in liquid phase was seen a reduction of the permeation flux through the sensors' membrane. However, a faster response for the helical geometry has been found, related to the higher S/V ratio, an important parameter to consider in permeation phenomena. A 2D model was developed trying to reproduce the trend of the probes and a good agreement was obtained for the gas phase experiments, with an error well below the 10 %. Moreover, a new similar device, Hyper-Quarch-II, will be built to characterise better the permeation sensors with multiple hydrogen partial pressure and temperature and to make a new measurement of the Sieverts' constant for lithium-lead.

The packed column technology has been tested in TRIEX-II facility in C. R. ENEA Brasimone between April and July 2019. Two operational mode have been analysed, one with hydrogen and one with deuterium. The helical permeation sensors were installed in the facility to test their performance in a complete lithium-lead loop and under operating conditions. The results obtained were quite scattered, because of the high times needed for stabilization in some tests and the inhomogeneities of the partial pressures readings. Extraction efficiencies obtained were lower than expected, but critical issues have been identified. The gas analysis at the outlet of the extractor allowed the evaluation of the extraction efficiency with a mass balance of the column. Unfortunately, the Sieverts' constant for

lithium-lead plays a key role in these calculations and the values found in literature are scattered among different order of magnitudes, leading to very different results. Also, the behaviour of the stripping gas was not well known in the extractor column, so that in some operative conditions helium and hydrogen bubbles could have been trapped in PbLi and released in the sensors box, leading to misleading readings. However, an increase in the extraction efficiency was seen with higher temperatures and higher PbLi flow rates. The 0D code developed for the mass balance of the system was compared with the results, but only few tests could be used. From the analysis done, it has been seen that the model has to be improved because of different trends of the concentrations of hydrogen respect to the real ones read. However, the code has proved useful to evaluate the order of magnitude of the permeation fluxes towards the environment. The maximum permeation fluxes are quite low, and the hydrogen released is well beyond the order of magnitude of the moles of hydrogen extracted with the packed column.

The Gas Liquid Contactor characterised in TRIEX-II show an extraction efficiency higher than expected, in particular using hydrogen in the purge gas of the extractor the efficiency increases thanks to the HD formation. The extracted Deuterium flux is one order of magnitude higher than in the extraction phase without hydrogen in the purge gas.

In conclusion, the packed column technology could be a good option for the TER system of ITER, but more experimental tests and efforts should be done. Particular attention should be posed in the characterisation of transport properties of lithium-lead, such as the solubility of hydrogen, and the development of suitable sensors to measure the concentration of solute and an appropriate probe's location in the loop to obtain the faster response and a higher accuracy of the readings.

Bibliography

[1] J.Freidberg, Plasma Physics and Fusion Energy, Cambridge University Press, 2007.

[2] K. M. M.Kikuchi, Fusion Physics, IAEA, 2012.

[3] D. Petkow, "ResearchGate". Available: https://www.researchgate.net/figure/Reaction-constants-for-different-fusion-reactions-7_fig1_283114377. [Accessed 3 July 2019].

[4] "FUSION FOR ENERGY". Available: https://f4e.europa.eu/understandingfusion/. [Accessed 3 July 2019].

[5] "U.S.NRC". Available: https://www.nrc.gov/reading-rm/doc-collections/fact-sheets/tritium-radiation-fs.html. [Accessed 3 July 2019].

[6] "ITER". Available: https://www.iter.org/proj/inafewlines. [Accessed 25 June 2019].

[7] "EURO FUSION". Available: https://www.euro-fusion.org/programme/demo/. [Accessed 1 July 2019].

[8] "CCFE - Culham Centre for Fusion Energy". Available: http://www.ccfe.ac.uk/Tokamak.aspx. [Accessed 25 June 2019].

[9] J. Wesson, "The Science of JET," 1999.

[10] "ITER". Available: https://www.iter.org/mach/vacuumvessel. [Accessed 25 June 2019].

[11] "ITER". Available: https://www.iter.org/newsline/150/458. [Accessed 1 July 2019].

[12] "ITER". Available: https://www.iter.org/mach/magnets. [Accessed 25 June 2019].

[13] V. L. Tanna, "ResearchGate". Available: https://www.researchgate.net/figure/A-3-D-view-of-the-ITER-main-magnet-system_fig13_34438815. [Accessed 1 July 2019].

[14] "ITER". Available: https://www.iter.org/mach/divertor. [Accessed 25 June 2019].

[15] "ITER". Available: https://www.iter.org/newsline/274/1639. [Accessed 1 July 2019].

[16] "ITER". Available: https://www.iter.org/mach/blanket. [Accessed 25 June 2019].

[17] L. M. Giancarli, M. Abdou and D. J. Campbell, "Overview of the ITER TBM Program," *Fusion Engineering and Design,* vol. 87, pp. 395-402, 2012.

[18] L. M. Giancarli, M.-Y. Ahn and I. Bonnett, "ITER TBM Program and associated system engineering," *Fusion Engineering and Design* , vol. 136, pp. 815-821, 2018.

[19] "ITER". Available: https://www.iter.org/mach/cryostat. [Accessed 25 June 2019].

[20] G. Federici, C. Bachmann and L. Barucca, "DEMO design activity in Europe: Progress and updates," *Fusion Engineering and Design,* vol. 136, pp. 729-741, 2018.

[21] J. Aubert, G. Aiello, P. Arena and T. Barrett, "Status of the EU DEMO HCLL breeding blanket design development," *Fusion Engineering and Design,* vol. 136, pp. 1428-1432, 2018.

[22] G. Federici, L. Boccaccini and F. Cismondi, "An overview of the EU breeding blanket design strategy as an integral part of the DEMO design effort," *Fusion Engineering and Design,* vol. 141, pp. 30-42, 2019.

[23] B. Bornschein, C. Day, D. Demange and T. Pinna, "Tritium management and safety issues in ITER and DEMO breeding blankets," *Fusion Engineering and Design,* vol. 88, pp. 466-471, 2013.

[24] R. Aymar, P. Barabaschi and Y. Shimomura, "The ITER design," *Plasma Physics and Controlled Fusion,* vol. 44, pp. 519-565, 2002.

[25] D. Demange, C. Alecu, N. Bekris and e. al., "Overview of R&D at TLK for process and analytical issues on tritium management in breeder blankets of ITER and DEMO," *Fusion Science and Technology,* vol. 87, pp. 1206-1213, 2012.

[26] A. Ciampichetti, F. S. Nitti, A. Aiello, I. Ricapito and e. al., "Conceptual design of tritium extraction system for the European HCPB Test Blanket Module," *Fusion Engineering and Design,* vol. 87, pp. 620-624, 2012.

[27] I. Ricapito, O. Bede, L. Boccaccini, A. Ciampichetti and e. al., "The ancillary systems of the European test blanket modules: configuration and integration in ITER," *Fusion Engineering and Design* , vol. 85, pp. 1154-1161, 2010.

[28] M. Utili, A. Ciampichetti and A. Aiello, "Design of a multipurpose laboratory scale apparatus for the investigation of hydrogen isotopes in PbLi and permeation technologies," *Fusion Engineering and Design,* vol. 87, pp. 1342-1346, 2012.

[29] K. Liger, X. Lefebvre and A. Ciampichetti, "HCLL and HCPB coolant purification system: design of the copper oxide bed," *Fusion Engineering and Design,* vol. 86, pp. 1859-1862, 2011.

[30] P. Humrickhouse, A. Ying and D. Rapisarda, "Tritium in DEMO," in *3rd IAEA DEMO Workshop*, ASIPP, Hefei, China, 13 May 2015.

[31] L. Candido, M. Utili, M. Zucchetti, A. Ciampichetti and P. Calderoni, "Development of advanced hydrogen permeation sensors to measure Q2 concentration in lead-lithium eutectic alloy," *Fusion Engineering and Design,* vol. 124, pp. 735-739, 2017.

[32] M. Utili, A. Ciampichetti, A. Aiello, I. Ricapito, P. Agostini, F. Desideri and K. Liger, "Design of a multipurpose laboratory scale apparatus for the

investigation of hydrogen isotopes in PbLi and permeation technologies," *Fusion Engineering and Design,* vol. 87, pp. 1342-1346, 2012.

[33] A. Ciampichetti, M. Zucchetti, I. Ricapito, M. Utili, A. Aiello and G. Benamati, "Performance of a hydrogen sensor in Pb-16Li," *Journal of Nuclear Materials* , Vols. 367-370, pp. 1090-1095, 2007.

[34] A. Ciampichetti, I. Ricapito, G. Benamati and M. Zucchetti, "Materials selection and design of a hydrogen measurement device in Pb-17Li," *Journal of Nuclear Materials,* Vols. 329-333, pp. 1332-1336, 2004.

[35] S. A. Steward, "Review of Hydrogen Isotope Permeability Through Materials," Livermore, California, 15 August 1983.

[36] H. J. Grabke and E. Riecke, "Absorption and Diffusion of Hydrogen in Steel," *Mater. Tehnol.,* vol. 34, pp. 331-342, 2000.

[37] M. Utili, M. Kordac, A. Venturini and L. Candido, "Deliverable D9_Final technical report FPA 372 SG04," 1 July 2019.

[38] F. Waelbroeck, P. Wienhold, J. Winter, E. Rota and T. Banno, Influence of bulk and surface phenomena on the hydrogen permeation through metals, Julich: Institut for Plasmaphysics Association EURATOM-KFA, 1984.

[39] P. W. Humrickhouse, "Permeation of multiple isotopes in the transition between surface- and diffusion-limited regimes," in *Tritium Focus Group meeting*, 25 September 2014.

[40] P. Humrickhouse, "Tritium Transport, Permeation, and Control," in *4th IAEA DEMO Programme Workshop*, 15 November 2016.

[41] M. A. Pick and K. Sonnenberg, "A Model for Atomic Hydrogen-Metal Interactions - Application to Recycling, Recombination and Permeation," *Journal of Nuclear Materials,* vol. 131, pp. 208-220, 1985.

[42] K. Kiuchi and R. B. McLellan, "The Solubility and Diffusivity of Hydrogen in Well-Annealed and Deformed Iron," *Acta metall.,* vol. 31, pp. 961-984, 1983.

[43] F. Reiter, "Solubility and diffusivity of hydrogen isotopes in Pb17Li," *Fusion Engineering and Design,* vol. 14, pp. 207-211, 1991.

[44] Y. C. Chan and E. Velckis, "A thermodynamic investigation of dilute solutions of hydrogen in liquid Li–Pb alloys," *Journal of Nuclear Materials,* Vols. 112-123, pp. 27-38, 1984.

[45] A. Aiello, A. Ciampichetti and G. Benamati, "Determination of hydrogen solubility in lead lithium using sole device," *Fusion Engineering and Design,* vol. 81, pp. 639-644, 2006.

[46] Y. Edao, H. Noguchi and S. Fukada, "Experiments of hydrogen isotope permeation, diffusion and dissolution in Li–Pb," *Journal of Nuclear Materials,* vol. 417, pp. 723-726, 2011.

[47] A.Aiello, A.Ciampichetti, M.Utili and G.Benamati, "TRIEX facility: An experimental loop to test tritium extraction system from lead lithium," *Fusion engineering and design* , vol. 82, pp. 2294-2302, 2007.

[48] M.Utili, A.Aiello, L.Laffi, A.Malavasi and I.Ricapito, "Investigation on efficiency of gas liquid contactor used as tritium extraction unit for HCLL-TBM Pb-16Li loop," *Fusion Engineering and Design* , Vols. 109-111, pp. 1-6, 2016.

[49] N. Alpy and A. T. T. Dufrenoy, "Hydrogen extraction from Pb-17Li: test with a packed column," *Fusion Engineering and Design,* Vols. 39-40, pp. 787-792, 1998.

[50] N. Alpy, A. Terlain and V. Lorentz, "Hydrogen extraction from Pb-17Li: results with 800 mm high packed column," *Fusion Engineering and Design,* Vols. 49-50, pp. 775-780, 2000.

[51] D. W. Green and R. H. Perry, "Equipment for Distillation, Gas Absorption, Phase Dispersion and Phase Separation," in *Perry's Chemical Engineers Handbook*, McGraw-Hill, 2008.

[52] B. K. Dutta, Principle of Mass Transfer and Separation Processes, Nuova Delhi: Prentice-Hall of India Private Limited, 2007.

[53] A. Bhargava, "Wet Scrubbers – Design of Spray Tower to Control Air Pollutants," *International Journal of Environmental Planning and Development,* vol. 2, 2016.

[54] K.Shimizu, S.Takada, K.Minekawa e Y.Kawase, «Phenomenological model for bubble column reactors: prediction of gas hold-ups and volumetric mass transfer coefficients,» *Chem. Eng. J.,* vol. 78, pp. 21-28, 2000.

[55] M. J. Angeles, C. Leyva, J. Anchyta and S. Ramirez. Available: https://www.researchgate.net/figure/Bubble-column-reactor_fig4_257402646. [Accessed 1 July 2019].

[56] "AMACS Process Tower Internals". Available: https://www.amacs.com/packing/random/. [Accessed 1 July 2019].

[57] "AMACS Proces Tower Internals". Available: https://www.amacs.com/what-is-structured-packing-and-how-is-it-used-in-process-plants/. [Accessed 1 July 2019].

[58] Costello, "Costello Consulting Engineers". Available: http://rccostello.com/wordpress/distillation/distillation-part-1-packed-towers-vs-tray-plate-towers/.

[59] EuroslotPars. Available: http://euroslotpars.com/en/products/packed-column/.

[60] J. F. Richardson, J. H. Harker and J. R. Backhurst, "Absorption of Gases - Chapter 12," in *Coulson and Richardson's Chemical Engineering - Volume 2*, Butterworth-Heinemann, 2002.

[61] J. F. Richardson, J. H. Harker and J. R. Backhurst, "Separation Columns (Distillation, Absorption and Extraction) - Chapter 11," in *Coulson and Richardson's Chemical Engineering - Volume 6*, Butterworth-Heinemann, 2005.

[62] T. Terai, S. Nagai and T. Yoneoka, "Mass Transfer Coefficient of Tritium from Molten Lithium-Lead Alloy (Li17Pb83) to Environmental Gas under

Neutron Irradiation," *Fusion Engineering and Design*, vol. 17, pp. 237-241, 1991.

[63] M. Utili, "Sizing of TEU and cold trap," Internal Deliverable D2.1 no. RT-OMF331 L2 T01-05, 2014.

[64] M. Utili, M. Kordac, A. Venturini and L. Candido, "Final technical report, D9-F4E-FPA-372: SG04," 1 July 2019.

[65] "SULZER". Available: https://www.sulzer.com/en/shared/products/2017/03/28/13/25/mellapak-and-mellapakplus.

[66] MathWorks, "MathWorks". Available: https://it.mathworks.com/.

[67] A. W. M. van Schijndel, "Implementation of COMSOL Multiphysics® in Simulink® S-Functions, Revisited," in *In Proceedings of the Comsol Conference Cambridge*, Cambridge, UK, 17-19 September 2014.